Estimation of aquifers hydraulic parameters by three different techniques: geostatistics, correlation and modeling.

PhD Thesis

Hydrogeology Group (GHS)

Dept Geotechnical Engineering and Geosciences, Universitat Politecnica de Catalunya, UPC-BarcelonaTech
Institute of Environmental Assessment and Water Research (IDAEA), Spanish Research Council (CSIC)

Author:
Marco Barahona-Palomo

Advisors:
Dr. Xavier Sánchez-Vila
Dr. Daniel Fernández-García

February, 2014

This thesis was co-funded by the University of Costa Rica (UCR) and the Spanish National Research Council (CSIC). Additional funding was provided by the Spanish Ministry of Science and Innovation through projects Consolider-Ingenio 2010 CSD2009-00065 and FEAR CGL2012-38120.

ABSTRACT

Characterization of aquifers hydraulic parameters is a difficult task that requires field information. Most of the time the hydrogeologist relies on a group of values coming from different test to interpret the hydrogeological setting and possibly, generate a model. However, getting the best from this information can be challenging.

In this thesis, three cases are explored. First, hydraulic conductivities associated with measurement scale of the order of 10^{-1} m and collected during an extensive field campaign near Tübingen, Germany, are analyzed. Estimates are provided at coinciding locations in the system using: the empirical Kozeny-Carman formulation, providing conductivity values, based on particle size distribution, and borehole impeller-type flowmeter tests, which infer conductivity from measurements of vertical flows within a borehole. Correlation between the two sets of estimates is virtually absent. However, statistics of the natural logarithm of both sets at the site are similar in terms of mean values and differ in terms of variogram ranges and sample variances. This is consistent with the fact that the two types of estimates can be associated with different (albeit comparable) measurement (support) scales. It also matches published results on interpretations of variability of geostatistical descriptors of hydraulic parameters on multiple observation scales. The analysis strengthens the idea that hydraulic conductivity values and associated key geostatistical descriptors inferred from different methodologies and at similar observation scales (of the order of tens of cm) are not readily comparable and should not be embedded blindly into a flow (and eventually transport) prediction model.

Second, a data-adapted kernel regression method, originally developed for image processing and reconstruction is modified and used for the delineation of facies. This

non-parametric methodology uses both the spatial and the sample value distribution, to produce for each data point a locally adaptive steering kernel function, self-adjusting the kernel to the direction of highest local spatial correlation. The method is shown to outperform the nearest-neighbor classification (NNC) in a number of synthetic aquifers whenever the available number of data is small and randomly distributed. Still, in the limiting case, when the domain is profusely sampled, both the steering kernel method and the NNC method converge to the true solution. Simulations are finally used to explore which parameters of the locally adaptive kernel function yield optimal reconstruction results in typical field settings. It is shown that, in practice, a rule of thumb can be used to get suboptimal results, which are best when key prior information such as facies proportions is used.

Third, the effect of water temperature fluctuation on the hydraulic conductivity profile of coarse sediments beneath an artificial recharge facility is model and compared with field data. Due to the high permeability, water travels at a high rate, and therefore also water with different temperature is also present on the sediment under the pond at different moments, this translates into different hydraulic conductivity values within the same layer, even though all the other parameters are the same for this layer. Differences of almost 79% in hydraulic conductivity were observed for the model temperatures (2 °C – 25 °C). This variation of hydraulic conductivity in the sediment below the infiltration pond when water with varying temperature enters the sediment, causes the infiltration velocity to change with time and produces the observed fluctuation on the field measurements.

RESUMEN

La caracterización de los parámetros hidráulicos de los acuíferos es una tarea difícil que requiere información de campo. La mayoría de las veces el hidrogeólogo se basa en un grupo de valores procedentes de diferentes pruebas para interpretar la configuración hidrogeológica y posiblemente , generar un modelo . Sin embargo, obtener lo mejor de esta información puede ser un reto.

En esta tesis se analizan tres casos. Primero, se analizan las conductividades hidráulicas asociadas a una escala de medición del orden de 10 m^{-1} y obtenidas durante una extensa campaña de campo cerca de Tübingen, Alemania. Las estimaciones se obtuvieron en puntos coincidentes en el sitio, mediante: la formulación empírica de Kozeny - Carman, proporcionando valores de conductividad, con base en la distribución de tamaño de partículas y las pruebas del medidor de caudal de tipo impulsor en el pozo, el cual infiere las medidas de conductividad a partir de los flujos verticales dentro de un pozo. La correlación entre los dos conjuntos de estimaciones es prácticamente ausente. Sin embargo, las estadísticas del logaritmo natural de ambos conjuntos en el lugar son similares en términos de valores medios y difieren en términos de rangos del variograma y varianzas de muestra. Esto es consecuente con el hecho de que los dos tipos de estimaciones pueden estar asociados con escalas de apoyo de medición diferentes (aunque comparables). También coincide con los resultados publicados sobre la interpretación de la variabilidad de los descriptores geoestadísticos de parámetros hidráulicos en múltiples escalas de observación . El análisis refuerza la idea de que los valores de conductividad hidráulica y descriptores geoestadísticos clave asociados al inferirse de diferentes metodologías y en las escalas de observación similares (en el caso

del orden de decenas de cm) no son fácilmente comparables y debe ser utilizados con cuidado en la modelación de flujo (y eventualmente, el transporte) del agua subterránea.

En segundo lugar, un método de regresión kernel adaptado a datos, originalmente desarrollado para el procesamiento y la reconstrucción de imágenes se modificó y se utiliza para la delimitación de las facies. Esta metodología no paramétrica utiliza tanto la distribución espacial como el valor de la muestra, para producir en cada punto de datos una función kernel de dirección localmente adaptativo, con ajuste automático del kernel a la dirección de mayor correlación espacial local. Se demuestra que este método supera el NNC (por su acrónimo en inglés *nearest-neighbor classification*) en varios casos de acuíferos sintéticos donde el número de datos disponibles es pequeño y la distribución es aleatoria. Sin embargo, en el caso límite, cuando hay un gran número de muestras, tanto en el método kernel adaptado a la dirección local como el método de NNC convergen a la solución verdadera. Las simulaciones son finalmente utilizadas para explorar cuáles parámetros de la función kernel localmente adaptado dan resultados óptimos en la reconstrucción de resultados en escenarios típicos de campo. Se demuestra que, en la práctica, una regla general puede ser utilizada para obtener resultados casi óptimos, los cuales mejoran cuando se utiliza información clave como la proporción de facies.

En tercer lugar, se modela el efecto de la fluctuación de la temperatura del agua sobre la conductividad hidráulica de sedimentos gruesos debajo de una instalación de recarga artificial y se compara con datos de campo. Debido a la alta permeabilidad, el agua se desplaza a alta velocidad alta, y por lo tanto, agua con temperatura diferente también está presente en el sedimento bajo el estanque en diferentes momentos, esto se traduce en diferentes valores de conductividad hidráulica dentro de la misma capa, a pesar de que todos los demás parámetros son los mismos para esta capa. Se observaron

diferencias de casi 79 % en la conductividad hidráulica en el modelo, para las temperaturas utilizadas (2 º C - 25 º C). Esta variación de la conductividad hidráulica en el sedimento por debajo de la balsa de infiltración cuando el agua de temperatura variable entra en el sedimento, causa un cambio en la velocidad de infiltración con el tiempo y produce las fluctuacciones observadas en las mediciones de campo.

ACKNOWLEDGEMENTS

Special thanks to my advisor Dr. Xavier Sánchez-Vila and co-advisor Dr. Daniel Fernández-García for their guidance, constant support and continuous motivation. I would also like to thank the Hydrogeology Group from the UPC-IDAEA, especially to Ms. Teresa García and Ms. Silvia Aranda. To my office mates and friends Estanis, Anna, Francesca, Daniele for being there and making my stay in Barcelona a more enjoyable experience, also to Diogo, Cristina, Manuela, Meritxell, Eduardo, Pablo, Carme, Jordi F., and many more that gave me a hand when needed. Gràcies nois!

To the people from CETAQUA for their collaboration in obtaining information used in chapter 4.

I am further thankful to my family and friends for their support and patience; special thanks to my family in Mexico for their constant support in many ways and to my parents for their love, endless support and encouragement.

I am also thankful to my dear wife for her extraordinary patience, understanding, and invaluable help to me in many ways whilst engaged in this work.

TABLE OF CONTENTS

LIST OF FIGURES

LIST OF TABLES

1. INTRODUCTION

1.1. MOTIVATION AND OBJECTIVES

Correlation of aquifer and aquitard materials can be challenging, due to the intrinsic heterogeneity in the geometry and genesis of the geological units and a general scarcity of data. Generating reliable hydrogeological data is both, time consuming and expensive, which makes impractical the efforts towards an exhaustive mapping of a given area and instead point measurements can be obtained by local-scale test in order to get representative values for the aquifer hydraulic parameters.

These tests or methods can take place on the field or at the lab, and each particular method may provide a different parameter estimate that can then be associated with the same location within the natural aquifer. Geostatistical methods provide a means for exploring the correlation structure, allowing comparisons of the results from different geological settings and providing information about spatial distribution of the hydraulic parameters that can be used in numerical groundwater flow models. The first goal of this thesis is to explore the degree of correlation between conductivity values associated with interpretation from two different methods (impeller flowmeter measurements and particle-size distributions (field and laboratory –based methods, respectively)) but for samples from the same location by means of basic statistics and key geostatistical parameters.

Generally, what the hydrogeologist has is a group of scattered data of hydraulic parameters (grain size, hydraulic conductivity, infiltration rates, etc.) from a given area; if there is not any other information available (i.e. a geology map) the first approach is to correlate those data by an interpolation method, that is, distinguishing the zone in areas of similar characteristics (i.e. facies). Many methods exist for scattered data interpolation (Franke, 1982), and some have been used for geologic facies reconstruction (i.e. Ritzi et al., 1994, Guadagnini et al., 2004, Tartakovsky & Wohlberg 2004, Wohlberg et al., 2006, Tartakovsky et al., 2007). The second goal of this thesis is to modified a non-parametric method (a data-adapted kernel regression function), designed for image processing (Takeda et al. 2007), and use it to create facies maps.

Daily water temperature fluctuation on surface water bodies is a common phenomenon due to environmental temperature changes; generally, natural water temperature variations can be of two types, seasonal variations (an annual cycle of low temperature during the winter and higher temperature during the summer) or daily fluctuations (generally higher temperature during day light and lower temperature at night). The effect of this temperature variation over groundwater recharge has been studied by some authors (Constantz et al., 1994, Constantz, 1998, Ronan et al. 1998, Lin et al., 2003; Braga et al., 2007) as hydraulic conductivity, K, is temperature dependent. The third goal of this thesis is to model the consequences that daily temperature variation has on the hydraulic conductivity profile beneath an infiltration pond with highly permeable soils comparing it with field data.

1.2. THESIS OUTLINE

This thesis is structured in five chapters, chapter 2 is based on a paper that has already been published, chapters 3 and 4 are based on papers that are in preparation; in chapter 5 major conclusions about those publications are presented. Each of these chapters focus on one of the objectives mentioned above. References to the papers are contained in a footnote at the beginning of each chapter.

A geostatistical comparison among the hydraulic conductivity results obtained by means of two popular techniques is presented in chapter 2; here, the values obtained via impeller flowmeter test and the particle size distribution at a decimetrical scale are compared using samples and measurements from a site near Tübingen, Germany. Estimates are provided at coinciding locations in the system using: (1) the empirical Kozeny-Carman formulation, providing conductivity values, K_{GS}, based on particle size distribution, and (2) borehole impeller-type flowmeter tests, which infer conductivity, K_{FM}, from measurements of vertical flows within a borehole. Correlation between the two sets of estimates is virtually absent. However, statistics of the natural logarithm of K_{GS} and K_{FM} at the site are similar in terms of mean values (averages of $ln\ K_{GS}$ being slightly smaller) and differ in terms of variogram ranges and sample variances. This is consistent with the fact that the two types of estimates can be associated with different (albeit comparable) measurement (support) scales. It also matches published results on interpretations of variability of geostatistical descriptors of hydraulic parameters on multiple observation scales. The analysis strengthens the idea that hydraulic conductivity values and associated key geostatistical descriptors inferred from different methodologies and at similar observation scales (of the order of tens of cm) are not readily comparable and should not be embedded blindly into a flow (and eventually transport) prediction model.

To generate punctual geological information can be both, expensive and time-consuming; therefore, most of the time geologist and hydrogeologists are faced with the task of generating conceptual geological maps or cross sections, interpreting scattered data collected in an area. In chapter 3, we explored a simple interpolation method to help on the delineation of facies, defined as the separation of geological units with distinct intrinsic characteristics (grain size, hydraulic conductivity, mineralogical composition, etc.). In the most frequent case in subsurface hydrology, when just a few scattered pieces of hydrogeological information are available, facies reconstruction becomes a major challenge. Several methods are available that can be used to achieve this task, ranging from those based only on existing hard data, to those including secondary data, or external knowledge about sedimentological patterns. Amongst those that are strictly based on hard data, the best results in terms of reconstructing synthetic images have been obtained with the nearest neighbor classification (NNC), a simple model that outperformed other more complex methodologies (e.g. support vector machine and indicator kriging). In this chapter, we present and test the results obtained for facies delineation when using a data-adapted kernel regression method, originally developed for image processing and reconstruction. This non-parametric methodology uses both the spatial and the sample value distribution, to produce for each data point a locally adaptive steering kernel function, self-adjusting the kernel to the direction of highest local spatial correlation. The method is shown to outperform NNC in a number of synthetic aquifers whenever the available number of data is small and randomly distributed. Still, in the limiting case, when the domain is profusely sampled, both the steering kernel method and the NNC method converge to the true solution. Simulations are finally used to explore which parameters of the locally adaptive kernel function

yield optimal reconstruction results in typical field settings. It is shown that, in practice, a rule of thumb can be used to get suboptimal results, which are best when key prior information such as facies proportions is used.

In chapter 4, head fluctuation in an artificial recharge pond is investigated, and a daily variation of the hydraulic conductivity in the sediment below the pond floor due to water with different temperature entering the pond is explored as the source of this fluctuation. Water temperature plays a major role on the groundwater–surface water interaction, this surface-water temperature fluctuation causes important variations on infiltration rates in streambeds. These variations are a consequence of variable density and viscosity with T. Thus, in some cases, water temperature has been pointed out as a proxy for infiltration rates estimation. In artificial recharge practices, though, this effect competes with the high infiltration rates, so that water effectively moves fast within the system, and the soil cannot ever be equilibrated with respect to temperature.

Data from a highly permeable infiltration pond (IP) located at an experimental site, show daily temperature and head fluctuation on surface-water. Infiltrating flow (Qout), obtained from mass balance, does not present the expected theoretical behavior of high infiltration rates due to high surface-water temperature or vice versa; furthermore, Qout temporal series seems to be out of phase with temperature. This apparently contradictory behavior is analyzed with a one-dimensional numerical model in an unsaturated medium, coupled with heat transport.

Observed daily temperature fluctuation on the pond-water, infiltrating through the vadose zone, is observed to have an increasing delay with depth this variation in temperature affects the hydraulic conductivity (due to viscosity and density dependence on T).

2. QUANTITATIVE COMPARISON OF IMPELLER-FLOWMETER AND PARTICLE-SIZE-DISTRIBUTION TECHNIQUES FOR THE CHARACTERIZATION OF HYDRAULIC CONDUCTIVITY VARIABILITY [1]

2.1. INTRODUCTION

Proper modeling of groundwater flow and subsurface transport requires assimilation of data on hydraulic parameters which are representative of scales that are relevant for the problem analyzed. Commonly used measurement and interpretation techniques are based on pumping tests. These typically provide equivalent or interpreted hydraulic parameters that are somehow integrated values within a given volume around the pumping and observation wells (e.g., Sanchez-Vila et al., 2006). While most of these interpreted values can be used to estimate the average flow behavior at some large scale, they can be of limited use for local-scale models, when a detailed characterization of spatial variability is needed. In particular, intermediate-scale models (*i.e.*, models involving horizontal length scales of the order of a few hundreds of meters) need a detailed knowledge of the architecture of the groundwater system together with the description of the small scale variability of parameters such as hydraulic conductivity, K, at scales ranging from the order of 10^{-1} to 10^{0} m. In this context, Riva et al. (2008,

[1] ***This chapter is based on the paper: Barahona-Palomo, M., Riva, M., Sanchez-Vila, X., Vazquez-Sune, E. and Guadagnini, A., 2011**, **Quantitative comparison of impeller-flowmeter and particle-size-distribution techniques for the characterization of hydraulic conductivity variability, Hydrogeology Journal, DOI: 10.1007/s10040-011-0706-5.***

2010) showed that a detailed geostatistical characterization based on sedimentological data collected at the centimeter scale was essential to provide a proper stochastically-based interpretation of the salient features of depth-averaged and multilevel breakthrough curves measured within an alluvial aquifer during a forced-gradient tracer test performed on a scale of about 50 m.

Historically, a number of methods have been proposed to obtain estimates of hydraulic parameters at scales of a few centimeters / decimeters. These methods can be typically divided into two categories: (1) field-, and (2) laboratory-based methods. The latter can be based on the analysis and interpretation of observations taken on undisturbed or disturbed samples. Each particular method may provide a different parameter estimate that can then be associated with the same location within the natural aquifer. Therefore, it is relevant to properly compare the characterization of the system ensuing from estimates of hydraulic parameters obtained with different interpretive methods but representative of support scales of the same order of magnitude.

Amongst the available techniques, the frequently used methods based on the analysis of (a) grain-size distribution (GSD) and (b) impeller flowmeter (IFM) information are particularly relevant. Particle-size distribution methods have been the focus of intense research since the late part of the XIX Century. Several compilations of empirical formulations developed to obtain hydraulic conductivity from particle-size distributions of soil samples are available (e.g., Vukovic & Soro, 1992; Fetter, 2001; Kasenow, 2002; Carrier, 2003; Odong, 2007; Riera et al., 2010). The idea of estimating local hydraulic conductivities with the aid of a flowmeter device was first proposed and developed in

the 1980s (e.g., Molz et al., 1989) to estimate hydraulic parameters in intermediate to high permeability formations. Some analyses have presented the main features of the GSD and IFM methodologies to obtain estimates of K at the small scale (e.g. Molz, et al., 1989; Wolf, et al., 1991; Hess, et al., 1992; Stauffer & Manoranjan, 1994; Boman, et al., 1997; Carrier, 2003; Odong, 2007). Qualitative comparisons between estimated conductivity values and associated key geostatistical parameters based on both methods can be found in the literature (e.g., Wolf et al., 1991; Stauffer and Manoranjan, 1994; Boman et al., 1997).

This work focuses on the impact that estimates of K obtained by means of (1) empirical formulations based on particle-size distributions and (2) in-situ hydraulic testing performed by borehole impeller flowmeters can have on the geostatistical characterization of spatial variability of hydraulic conductivity. It is emphasized that, while the measurement scale associated with particle-size-based methods is sufficiently clear, the precise definition of the support scale of flowmeter-based hydraulic conductivities is still lacking (e.g., Beckie, 1996; Zlotnik et al., 2000; Zlotnik and Zurbuchen, 2003a). Here, for the purpose of discussion it is assumed that the characteristic length scales of flowmeter measurements and GSD estimates, albeit different, are of the same order of magnitude of the borehole diameter, *i.e.* (10^{-1} m). It is with this spirit that the analyses and comparisons on a dataset collected in the alluvial unconfined aquifer of Tübingen, Germany, are performed. This dataset was partly used by Neuman et al. (2007, 2008) for the probabilistic interpretation of cross-hole pumping tests and for a multiscale geostatistical characterization of the aquifer. In the same experimental site, Riva et al. (2006, 2010) performed Monte Carlo-based analyses of a

tracer test. As detailed in section 2.3. *The Tübingen site dataset* below, GSD- and IFM-based *K* estimates are here available at a set of coinciding locations in the system. The analysis of the main statistics and key geostatistical parameters characterizing the heterogeneity of hydraulic conductivities estimated with GSD and IFM methods at the site is presented. The degree of correlation between *K* values obtained with the different methodologies examined is then explored. The results provide evidence of the lack of correlation between GSD- and IFM-based hydraulic conductivity values.

Comparisons similar to the one presented in this work were performed at the Savannah River Site, South Carolina (USA) (Boman et al., 1997) and at the Cape Cod Site, USA (Hess et al., 1992). In the former site both IFM- and GSD-based *K* measurements/estimates taken along adjacent boreholes (*i.e.*, boreholes were separated only by a few meters distance) were available. In the latter, hydraulic conductivity data coming from field and laboratory experiments, respectively based on IFM-measurements and permeameter tests performed on undisturbed samples, were compared. As opposed to these works, it is remarked that the data set here analyzed comprises a large number of data points collected with GSD- and IFM-based methods at coinciding locations.

2.2. METHODOLOGY

For completeness and ease of reference, the salient features of the IFM and GSD methodologies used to estimate small scale hydraulic conductivity values are briefly reviewed.

2.2.1. ESTIMATES OF HYDRAULIC CONDUCTIVITY FROM IMPELLER FLOWMETER (IFM) DATA

The borehole flowmeter methodology was developed and presented by Hufschmied (1986), Rehfeldt et al. (1989) and Molz et al. (1989). The technique relies on pumping at a fixed rate from a screened well to attain (approximately) horizontal flow in the surrounding of the well and vertical flow within the well bore. The distribution of horizontal hydraulic conductivity along the borehole is then based on measured values of the vertical distribution of discharge within the pumping well. The latter are taken by means of a down-hole impeller flowmeter. The flowmeter probe is initially positioned at the bottom of the screened interval while pumping. It is then systematically moved upwards and is maintained at a given depth until a stable velocity recording is obtained. The vertical distribution of hydraulic conductivity is then obtained according to (Molz et al., 1989; Molz et al., 1994)

$$\frac{K_{FM,i}}{\bar{K}} = \frac{\Delta Q_i / Q_P}{\Delta b_i / B} \qquad \text{(Equation 2.1)}$$

Here, $\bar{K}$ is the average hydraulic conductivity estimated at the site, *e.g.*, from a pumping test; Q_P is the total pumping rate from the well; B is the screened thickness of the aquifer; ΔQ_i is the discharge measured within the i-th sampling interval of vertical thickness Δb_i; and $K_{FM,i}$ is the estimated value for the hydraulic conductivity representative of the sampled i-th vertical interval. Perfect layering of the aquifer system in the proximity of the well is a key assumption at the basis of (Equation 2.1).

Critical points in the interpretation of field information also include well losses (Rehfeldt et al., 1989; Molz et al., 1989). With reference to electromagnetic borehole flowmeters and following an observation by Boman et al. (1997), Zlotnik and Zurbuchen (2003b) showed that neglecting head losses can lead to biased interpretations. Young (1998) showed that positive skin effects can influence the data analysis based on (Equation 2.1) at wells without gravel packs located at Columbus Air Force Base, Mississippi (USA). On the other hand, the presence of a gravel pack mitigated these effects.

Molz et al. (1989) presented a comparison between the vertical distribution of hydraulic conductivity, $K_{FM}(z)$ (z being the vertical coordinate), obtained by IFM and conductivity estimates obtained by other methods, such as tracer tests and multilevel slug tests, at a field site near Mobile, Alabama (USA). They concluded that, although hydraulic conductivities obtained by these three methods were not identical, they displayed similar spatial patterns. The authors point out that the assumption of a layered, stratified aquifer in the proximity of the pumping well limits the proper characterization of the unknown three-dimensional distribution of K. Several additional studies have been published on intercomparisons between hydraulic conductivity estimates based on the IFM technique and other methods, including dipole flow tests, multilevel slug tests, and permeameter tests (Wolf et al., 1991; Hess et al., 1992; Zlotnik and Zurbuchen, 2003a; Butler, 2005). With specific reference to comparisons between IFM- and GSD-based conductivity estimates, Whittaker and Teutsch (1999) perform numerical analyses on a hypothetical aquifer and study the impact that simulated flowmeter information and sieve analyses of cores have on the travel times of tracer particles. The authors observed

that, whilst the Gaussian simulations based on sieve analyses were better able to represent high permeability lenses and therefore better reproduced the variability of the exhaustive data set, this did not lead to a better prediction of the arrival times of particles. On the contrary, simulations based on data extracted from flowmeter measurements were consistently more accurate, despite their failure to generate regions of high permeability.

2.2.2. ESTIMATES OF HYDRAULIC CONDUCTIVITY FROM GRAIN-SIZE DISTRIBUTIONS (GSD)

It is well accepted that hydraulic conductivity is related to the particle-size distribution of granular porous media. An estimate of the hydraulic conductivity of a sample can then be obtained by using information on particle size distributions in empirical relationships (compilations of several existing relationships can be found, e.g., in Vukovic and Soro, 1992; Odong, 2007; Cheng and Chen, 2007; Payne et al., 2008, and references therein).

Grain-size-based methods are typically applied to porous medium samples and the estimates are assumed to be independent on flow configuration. These methods are appealing for the estimation of hydraulic conductivity because sieve analysis practices are well established procedures in groundwater investigations and can be performed with a moderate experimental effort. Hydraulic conductivity estimates based on GSD

information, K_{GS}, provided by a series of empirical methods can be synthesized by the following relationship

$$K_{GS} = \frac{g}{\nu} C\, f(\phi)\, d_e^2 \qquad \text{(Equation 2.2)}$$

where g is gravity acceleration, ν is the kinematic viscosity of the fluid, $f(\phi)$ is a function of porosity, ϕ, d_e is an effective grain diameter, and C is defined as a sorting coefficient. The values of C, and d_e, and the type of relationship, $f(\phi)$, depend on the formulation adopted. When applied to the same sample, the different existing empirical relationships provide estimates of permeability that could span more than one or two orders of magnitude (Custodio and Llamas, 1984; Fogg et al., 1998; Riera et al., 2010). A widely used formulation is that of Kozeny-Carman, where

$$C = 8.3\times10^{-3}; \quad f(\phi) = \left[\frac{\phi^3}{(1-\phi)^2}\right]; \; d_e = d_{10} \qquad \text{(Equation 2.3)}$$

Here, d_{10} is the grain diameter (in mm) that corresponds to 10% (by weight) of the soil sample passing, and K_{GS} is given in m/day. Using (Equation 2.2) requires that porosity measurements be available. In case ϕ measurements are not directly available, an estimate of ϕ could be obtained by means of the following empirical formula (e.g., Vukovic and Soro, 1992)

$$\phi = 0.255\left(1 + 0.83^{U}\right); \qquad U = \left(\frac{d_{60}}{d_{10}}\right) \qquad \text{(Equation 2.4)}$$

where d_{60} is the grain diameter that corresponds to the 60% (by weight) of the sample passing, and U is the coefficient of uniformity. It is remarked that, as a result of sample homogenization which might occur during particle size analysis, values based on GSD methods can be considered as lying in between the two components along the principal

directions of the local conductivity tensor (vertical and horizontal if layers are not tilted).

The Kozeny-Carman equation has been applied to a large variety of fine and coarse-grain sediments, ranging from non-plastic, cohesionless silts to sand and gravel mixtures (Carrier, 2003; Gallardo and Marui, 2007; Odong, 2007; Wilson et al., 2008). The method is less reliable for very-poorly sorted soils, or soils with highly irregular shapes (Carrier, 2003), as well as for plastic soils (with significant clay or organic content, where fabric, destroyed by disturbance of the sample, influences hydraulic conductivity) or well-sorted cobble-sized gravel. As a general rule, the Kozeny-Carman equation provides good estimates of K whenever d_{10} ranges between approximately 0.1 and 3.0 mm. Odong (2007) assessed the reliability of several competing empirical equations to estimate hydraulic conductivity from grain size distributions of unconsolidated aquifer materials and concluded that the best overall estimation of K is obtained by means of the Kozeny-Carman formula. Carrier (2003) and Barr (2005) have performed similar comparisons supporting the same conclusion. Examples of acceptable correlation between GSD K estimates and hydraulic tests have been documented by Zlotnik and McGuire (1998) and Cardenas and Zlotnik (2003).

2.3. THE TÜBINGEN SITE DATASET

The Tübingen aquifer consists of alluvial material overlain by stiff silty clay and underlain by hard silty clay. The lithostratigraphic characterization has been performed on the basis of the stratigraphy obtained from 150 mm-diameter monitoring wells

(Sack-Kühner, 1996; Martac and Ptak, 2003) and from one 400 mm-diameter pumping well. All wells were drilled to the marly bedrock constituting the impermeable aquifer bottom of variable depth and are surrounded by a gravel pack. The aquifer saturated thickness is about 5 m. Extensive field and laboratory scale aquifer investigation procedures were performed at the site, including grain sieve analyses, down-hole impeller flowmeter measurements and pumping tests. The sieve analyses were performed on drill core samples ranging in length from 5 to 26.5 cm and indicated very heterogeneous, highly conducive alluvial deposits. More than 400 grain distribution curves are available within the test area, distributed along 12 vertical boreholes, providing sufficient information to estimate hydraulic conductivity values, K_{GS}, from (Equation 2.2) – (Equation 2.4). A total of 312 K_{FM} measurements are available within the same wells. These were collected without installing packers in the wells. A thin rubber seal was placed around the impeller-type probe to increase its sensitivity to flow. Due to the small mean velocity head within the borehole, concentrated hydraulic losses associated with the device were not considered in the data interpretation. Measurements are related to vertical intervals with lengths ranging from 3 to 40 cm. The latter are of the similar order of magnitude of a typical length scale of the support (measurement) scale associated with samples on which the GSD-based interpretations are obtained. Table 1 reports the spatial coordinates of the locations of the boreholes where measurements have been performed, together with the main characteristics of the flowmeter data. The table also includes the number of flowmeter and grain-size distribution data, N_{IFM} and N_{GSD} respectively. It is noted that it is possible to obtain both GSD and IFM conductivity information at N_{MATCH} = 112 coinciding locations in the system. In this work, 'coinciding locations' means a match that considers (a) the length and absolute location of a sample from which GSD has been analyzed, and (b) the

location along the vertical of the impeller flowmeter. If the GSD location falls within the interval determined in (b), then the two locations are considered coinciding. This constitutes a rather unique three-dimensional data-set which allows exploring extensively the relationship between the interpretations based on these two types of measurements.

Table 2-1. x and y in Gauβ-Krüger coordinates, of the boreholes at the Tübingen site. Main characteristics of the flowmeter data: L (length of the vertical interval investigated); Δz_{min}, Δz_{max} (minimum and maximum distance between packers); d_1, d_2 (distances between the ground level and the first and last packer); Z_{max}, Z_{min} (vertical elevations of the highest and lowest packers). Number of data available: N_{IFM} (IFM measurements); N_{GSD} (GSD measurements); N_{MATCH} (number of IFM and GSD data taken at the same vertical elevation within a borehole).

Borehole	x	y	L (m)	Δz_{min} (m)	Δz_{max} (m)	d_1 (m)	d_2 (m)	Z_{max} (m a.s.l)	Z_{min} (m a.s.l)	N_{IFM}	N_{GSD}	N_{MATCH}
F0	3508686	5377739	1.40	0.05	0.15	5.06	6.46	304.52	303.02	15	12	4
F1	3508629	5377746	2.19	0.05	0.20	4.74	6.73	305.90	303.71	13	10	2
F2	3508680	5377687	2.34	0.05	0.15	4.40	6.67	305.99	303.65	23	20	6
F3	3508586	5377660	0.69	0.05	0.10	8.72	9.30	301.83	301.34	9	12	0
F4	3508419	5377670	1.47	0.05	0.15	4.48	5.86	306.70	305.23	15	9	0
F5	3508459	5377622	2.45	0.05	0.15	4.25	6.60	306.60	304.25	23	14	8
F6	3508500	5377574	0.60	0.05	0.10	3.90	4.40	306.71	306.16	7	18	0
B1	3508702	5377754	0.80	0.05	0.25	4.17	4.92	305.08	304.32	8	59	7
B2	3508703	5377759	1.85	0.03	0.06	3.98	5.78	305.35	303.55	32	55	15
B3	3508712	5377757	3.06	0.04	0.40	3.42	6.43	305.48	302.47	41	67	20
B4	3508691	5377769	4.85	0.05	0.35	3.55	8.32	305.86	301.08	65	69	36
B5	3508703	5377779	3.45	0.05	0.30	3.38	6.78	305.82	302.42	61	62	14
									Total	312	407	112

2.4. DATA ANALYSIS AND DISCUSSION

The three-dimensional distributions of hydraulic conductivity estimates obtained by GSD and IFM interpretations at the site are here presented and discussed in terms of basic univariate statistics and a detailed geostatistical analysis of the available data is performed. The degree of correlation between the different types of measurements at the site is then assessed.

2.4.1. UNIVARIATE STATISTICS AND GEOSTATISTICAL ANALYSIS OF THE DATA-SET

Riva et al. (2006) present a geostatistical analysis of the hydraulic conductivity values calculated from grain sieve curves by means of the Beyer's model (Beyer, 1964). On the basis of section 2.2.2. *Estimates of hydraulic conductivity from grain-size distributions (GSD),* these are interpreted by using (Equation 2.2) – (Equation 2.4). A high correlation (not shown) was found between the conductivity values obtained with these two empirical models. For completeness, the key statistics of the measured distributions of d_{10} and d_{60} are reported in appendix A.

Uncertainty u_K associated with conductivity values estimated on the basis of (Equation 2.2) – (Equation 2.4) and related due to uncertainties in measured d_{10} and d_{60} can be assessed by the following relationship (e.g., International Organization of Standardization-GUM, 1995)

$$u_K = \sqrt{\sum_i \left(\frac{\partial K}{\partial d_i} \right)^2 (u_{d_i})^2} \qquad i = 1, 2 \qquad \text{(Equation 2.5)}$$

where d_1 and d_2 respectively would be d_{10} and d_{60} and u_{d_i} is the measurement uncertainty of d_i. The latter has been estimated to be less than 2% by the American Association for Laboratory Accreditation (2005). In this case, however, a conservative 2% value is used for the estimation of the uncertainty. For simplicity, it is assumed that the quantities which were treated as constant in (Equation 2.2) – (Equation 2.4) (including gravity and physical properties of the fluid) are provided without uncertainty. On this basis, the uncertainty u_K was calculated to be less than 10% for 95% of the total number of samples. Uncertainty associated with IFM estimates of conductivity can then be derived on the basis of (Equation 2.1). This is however a delicate task, because, in addition to typical measurement uncertainties associated with pumping flow rates and length scales included in (Equation 2.1), one should also take into account the implications of the conceptual model adopted for the system. These analyses are seldom performed in the field with this degree of detail. For simplicity and for the sake of the demonstration example here, the matter is not pursued further in this work. Additional details related to the uncertainty analysis performed are reported in appendix A.

Sample histograms of the natural logarithm of all available hydraulic conductivity data, $Y = ln\ K$ (conductivities are measured in m/s), estimated by means of IFM and GSD techniques are depicted in Figure 2-1. A summary of basic univariate statistics is presented in Table 2 for the complete data-sets and for the subsets of conductivity values estimated only at the $N_{MATCH} = 112$ points where GSD and IFM data are jointly available. It is noted that both methods lead to average hydraulic conductivity values of the same order of magnitude, the GSD-based averages being slightly smaller than their IFM-based counterparts. They render different frequency distributions and log-conductivity variance, that of $ln\ K_{GS}$ being larger than that of $ln\ K_{FM}$.

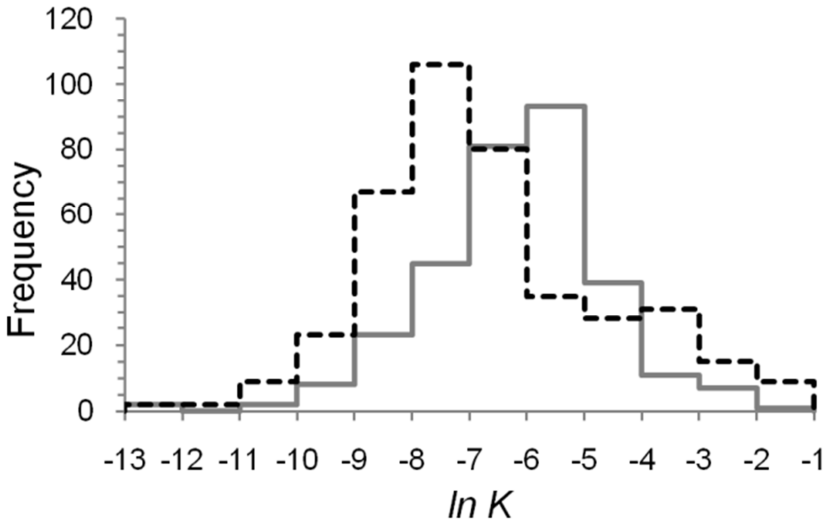

Figure 2-1. Histograms of frequency distribution for ln KFM (continuous gray line) and ln KGS (discontinuous black line) values when all available points are used. Number of available data points is 312 for KFM and 407 for KGS.

Table 2-2. Basic univariate statistics for the complete Tübingen site data-sets and for the subsets of conductivity values estimated only at the N_{MATCH} = 112 points where GSD and IFM data are jointly available.

	IFM N_{IFM}	**IFM** N_{MATCH}	**GSD** N_{GSD}	**GSD** N_{MATCH}
Minimum *ln K*	-12	-10	-13	-9.3
Maximum *ln K*	-1.7	-3.6	-1.1	-1.5
Mean *ln K*	-6.2	-6.1	-6.7	-6.2
Median *ln K*	-6.1	-5.9	-7.1	-6.6
Standard Deviation of *ln K*	1.5	1.3	2.0	1.8
Skewness of *ln K* distribution	-0.33	-0.69	0.52	0.73
Mean *K* ($\times 10^{-3}$m/s)	6.8	4.4	12	12
Geometric mean of *K* ($\times 10^{-3}$ m/s)	2.1	2.3	1.2	2.0

Table 3 summarizes the results of the Kolmogorov-Smirnov (K-S) test performed at a significance level $\alpha = 0.05$ for the complete data-sets and for the subsets of data corresponding to the N_{MATCH} points. For completeness, Figure 2-2 reports normal probability plots for the four sample sets analyzed. The results evidence that the two sets of $ln\ K_{FM}$ data pass the K-S test at $\alpha = 0.05$, despite Figure 2-2a evidence that the subset of $ln\ K_{FM}$ values corresponding to the N_{MATCH} locations somehow undersamples the tail of the distribution corresponding to the largest conductivity values (this is also evidenced by the skewness values reported in Table 2). On the other hand, while the complete set of $ln\ K_{GS}$ data does not pass the K-S test of normality at $\alpha = 0.05$, the subset representing the N_{MATCH} locations does.

Table 2-3. Kolmogorov-Smirnov test parameters for the $ln\ K_{FM}$ and $ln\ K_{GS}$ data sets analyzed at the Tübingen site. All critical values are calculated for a significance level $\alpha = 0.05$.

	Number of points	**K-S measure**	**Critical value**
$ln\ K_{FM}$	N_{IFM}	0.060	0.077
$ln\ K_{FM}$	N_{MATCH}	0.074	0.129
$ln\ K_{GS}$	N_{GSD}	0.096	0.067
$ln\ K_{GS}$	N_{MATCH}	0.111	0.129

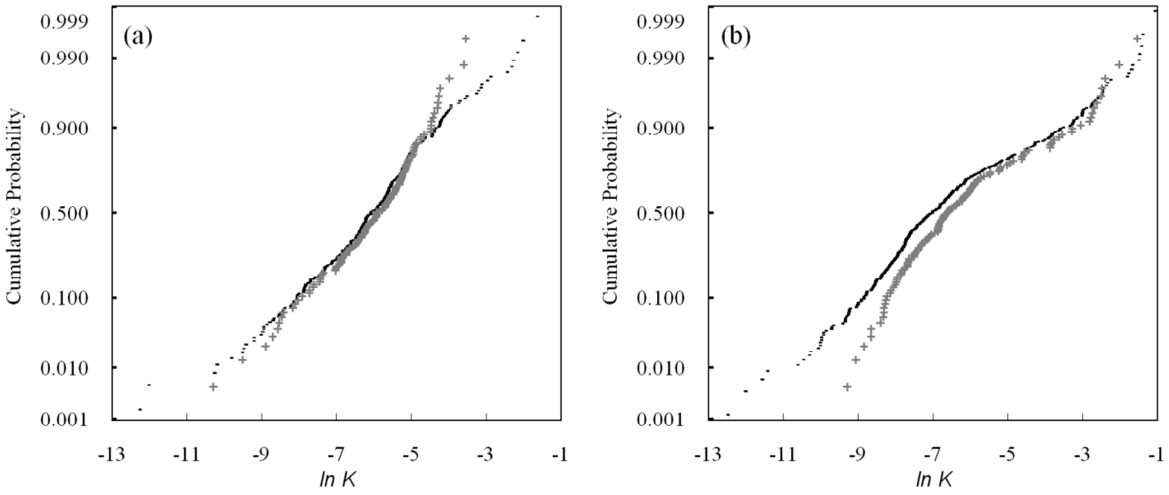

Figure 2-2. Normal probability plots for the *ln K* values obtained with (a) IFM and (b) GSD methods at the Tübingen site. Results obtained with the full data set and with data available at the N_{MATCH} locations are reported in *gray* and *black*, respectively

A t-test analysis was then performed to determine if the four data sets above mentioned can be considered as statistically different from each other. Table 4 summarizes the results of the tests performed upon analyzing different combinations of data sets pairs at a significance level α = 0.05. These analyses indicate that the two data sets corresponding to all K_{FM} and K_{GS} available measurements are not representative of samples belonging to the same population at the chosen significance level.

Table 2-4. Calculated t values for the t-test analysis. Critical values are calculated for a significance level α= 0.05.

			Test statistic	**Critical value**	**Result**
$ln\ K_{FM}^{m}$	vs	$ln\ K_{GS}^{m}$	0.627	1.96	Not significant
$ln\ K_{FM}^{a}$	vs	$ln\ K_{GS}^{a}$	3.974	1.96	Significant
$ln\ K_{FM}^{a}$	vs	$ln\ K_{FM}^{m}$	0.667	1.96	Not significant

$ln\ K_{GS}^{a}$	vs	$ln\ K_{GS}^{m}$	2.517	1.96	Significant

[a] = all data points; [m] = only matching points.

The observed differences suggest that, in general, GSD-based empirical formulations tend to provide estimates of *Y* which are characterized by a stronger spatial variability than those obtained by IFM methods.

A geostatistical analysis was then performed separately for hydraulic conductivities obtained from each method. Horizontal and vertical sample variograms have been constructed. Two-point statistics for a given separation lag are considered only if these are calculated on the basis of at least 50 data pairs. The choice of theoretical models to interpret variograms is based on visual inspection of experimental data. Estimation of variogram parameters was performed on the basis of visual inspection.

Figure 2-3 shows the horizontal and vertical sample variograms of log-conductivities derived from IFM and GSD analyses of all available data together with the corresponding theoretical models adopted. Table 5 reports the main results of the three-dimensional geostatistical analysis. The results indicate that IFM and GSD techniques lead to different geostatistical depictions of the spatial variability of *Y*. This is consistent with the results of the t-test presented above and supports the idea that the two datasets belong to different populations. The horizontal and vertical variograms of $ln\ K_{FM}$ are characterized by larger ranges and smaller sills than those associated with the variograms of $ln\ K_{GS}$, indicating a stronger spatial persistence than that offered by $ln\ K_{GS}$. It is noted that the sills of the vertical variograms are smaller than the

corresponding horizontal ones. This suggests that the total variance is mostly controlled by interwell (rather than intrawell) variability.

The reported findings are consistent with the fact that IFM- and GSD-based hydraulic conductivities can be interpreted as quantities associated with different, albeit of the same order of magnitude, support (measurement) scales. The former are somehow an average of the response of the system to a stress and reflect the local flow conditions around the well (including preferential paths, geological structures, effective porosity). The latter are only influenced by the local composition of the granular material and can display sharp spatial contrasts, giving rise to an enhanced interpreted variability of the system, with larger sills and shorter ranges than those associated with IFM interpretations. Note that this is not in contrast with the observation that the support scales of the two measurements are of the same order of magnitude. The pattern displayed by these observations is in line with published results about variability of geostatistical parameters of conductivity on multiple support scales (e.g., Tidwell and Wilson, 1999a, b; Neuman and Di Federico, 2003).

Table 2-5. Results of the three-dimensional geostatistical analysis of $Y = ln\ K$.

	$ln\ K_{FM}^{v}$	$ln\ K_{FM}^{h}$	$ln\ K_{GS}^{v}$	$ln\ K_{GS}^{h}$
Variogram type	Spherical	Spherical	Spherical	Spherical
Nugget	0.95	0.50	1.10	1.50
Range (m)	2.5	55	0.45	25
Sill	2.15	3.50	3.00	4.18

^{v} = vertical direction; ^{h} = horizontal direction

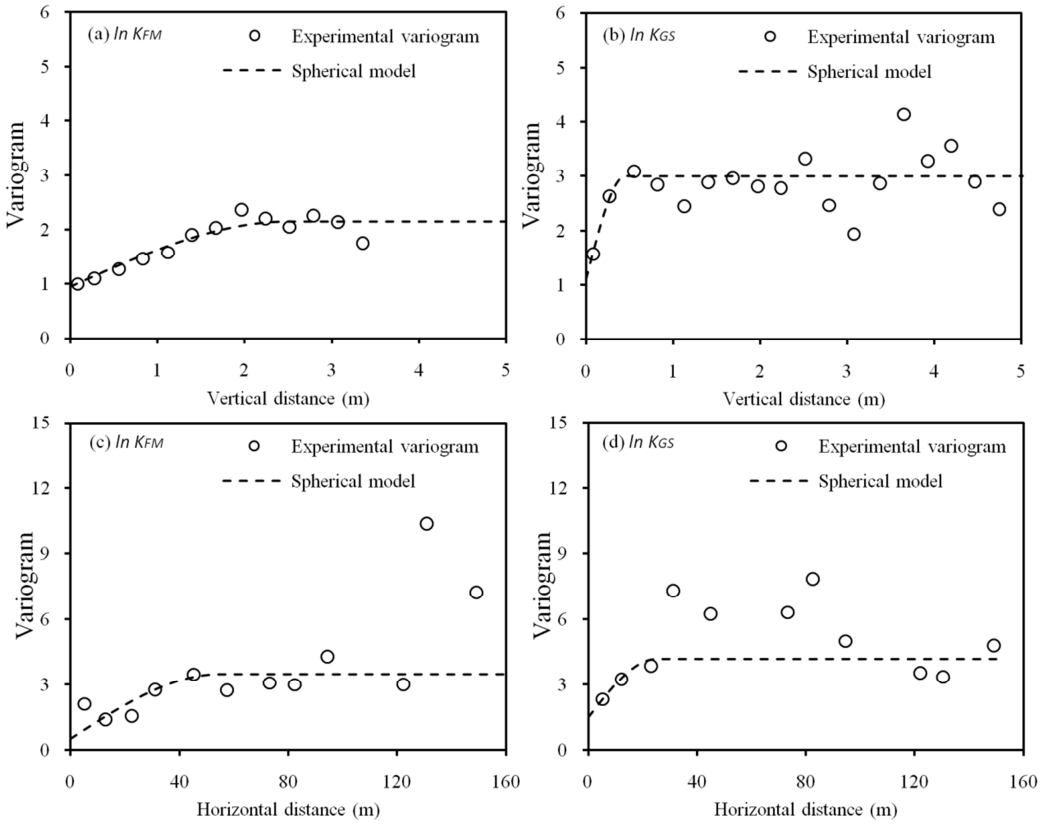

Figure 2-3. (a) Vertical variogram for *ln* K_{FM}, (b) Vertical variogram for ln K_{GS}, (c) Horizontal variogram for *ln* K_{FM}, and (d) Horizontal variogram for *ln* K_{GS}. *Dashed line* indicates the adopted variogram models.

2.4.2. CORRELATION BETWEEN DATA TYPES

The degree of correlation between *ln* K_{FM} and *ln* K_{GS} at the site is here explored, considering only *ln* K_{FM} and *ln* K_{GS} data at the N_{MATCH} locations. The scatter plot presented in Figure 2-4 shows the degree of correlation between these two variables. These results show that the *ln* K_{GS} values are weakly correlated with *ln* K_{FM}, the regression coefficient, R^2, being close to zero. The observed lack of correlation between

the IFM and GSD- based measurements is also consistent with the space-averaging effect associated with downhole flowmeters, as opposed to the more localized measurement offered by GSD interpretations, as discussed in section 2.4.1. *Univariate statistics and geostatistical analysis of the data-set*. These observations further corroborate the idea that the relationship between vertical fluxes measured by impeller flowmeters and the micro-structure of the system is still not clear and should be questioned and further analyzed in real site applications.

A possible explanation of the lack of correlation between the IFM and GSD- (or permeameter-) based measurements is that the former somehow average the response of the system to a stress and reflect the local flow conditions around the well (including preferential paths, geological structures, effective porosity). This might also be consistent with the observation that IFM conductivity estimates are associated with the lowest variances and largest mean values and ranges. On the other hand, K_{GS} and K_P are only influenced by the local composition of the granular material. The latter can display sharp spatial contrasts, giving rise to an enhanced interpreted variability of the system, with larger sills and shorter ranges than those associated with IFM interpretations.

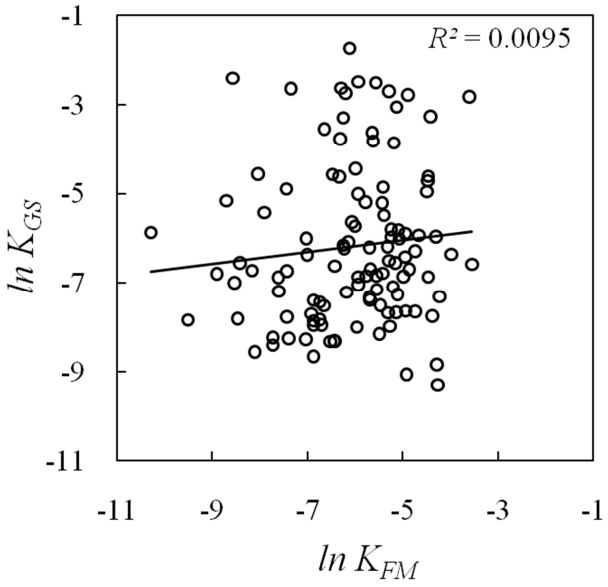

Figure 2-4. Scatter plot of the *ln K* values obtained by the flowmeter method and grain sieve analysis. A weak correlation is noticeable in the graph. The value of the regression coefficient, R^2, is reported.

2.5. CONCLUSIONS

A detailed analysis is presented of the basic statistics and key geostatistical parameters describing the three-dimensional spatial variability of hydraulic conductivities associated with measurement scales of the order of a few tens of cm within the alluvial aquifer located near the city of Tübingen, Germany. Hydraulic conductivities are obtained by means of impeller-type flowmeter measurements and particle-size sedimentological data at 112 coinciding locations in the system. The degree of correlation between conductivity values associated with interpretation methods based on impeller flowmeter measurements and particle-size distributions has then been explored. The work leads to the following major conclusions:

- The univariate statistical analysis of hydraulic conductivities estimated at the site highlights that the GSD-based average hydraulic conductivities are slightly smaller than their IFM-based counterparts. The analysis suggests that the variance of the natural logarithms of IFM estimates is smaller than that of GSD interpretations. From a statistical standpoint, the interpreted conductivities obtained with these methods appear to identify samples belonging to different populations.
- At the site, the IFM-based log-conductivity variograms are generally characterized by larger ranges and smaller sills than those relying on GSD interpretations. As such, they render a spatial distribution of log-conductivities associated with relatively large correlation scales, resulting in a more spatially persistent depiction of heterogeneity than that rendered by their GSD-based counterparts.
- Log-conductivity values based on particle-size information are essentially uncorrelated with their IFM counterparts at the site, with linear regression coefficient close to 0.0.
- The three previous conclusions can all be associated with the fact that the IFM method provides estimates within a given borehole that somehow smooth or dampen actual (small-scale) natural variability, because the pressure distribution around the measuring device can be far from the theoretical distribution envisioned for homogeneous systems. On the other hand, GSD-based conductivities are only influenced by the local composition of the tested granular material. The latter can display significant spatial contrasts, resulting in larger sills and shorter ranges than those associated with IFM interpretations. These findings are consistent with the fact that the two types of estimates analyzed can

be associated with different, albeit of similar order of magnitude, support (measurement) scales. Precise characterization of the support scale of any given information is thus needed to properly include hydraulic conductivity data into numerical models. This is particularly needed for the assessment of the support scale linked IFM conductivity measurement, which is still not completely clear.

- These results suggest that the relationship between vertical fluxes measured by impeller-type flowmeters and the micro-structure of the system is still not clear and should be tackled with great care in real site applications.

3. A LOCALLY ADAPTIVE KERNEL REGRESSION METHOD TO DELINEATE FACIES[2]

3.1. INTRODUCTION

Image reconstruction has a long history in a number of disciplines such as satellite image mapping, shape recognition in robotics, face recognition and license plate reading, among other uses (Bughin et al. 2008, Daoudi et al. 1999, Yang & Huang 1994, Lin & Chen 2008). The topic can be loosely subdivided into two main groups: (a) The reconstruction of incomplete images, where some of the pixels have no information so that pixel reconstruction is an inference problem; and (b) The reconstruction of noisy images, where some of the pixels display wrong information and the main problem is detecting and reclassifying the misclassified pixels.

A good reconstruction work relies heavily on the presence of data and on an efficient reconstruction algorithm that can either complete information gaps, or else filter noisy signals. A particular case of reconstruction appears in subsurface hydrology, where the amount of available information is small, so that the initial available picture for reconstruction is mostly a black signal (meaning no information) with some sparse data scattered throughout the medium. Data regarding facies distribution relies on very few points (well logs), and reconstruction is a really difficult and error prone task.

[2] ***This chapter is based on the paper: Barahona-Palomo, M., Fernàndez-Garcia, D., and Sanchez-Vila, X., 2013, A locally adaptive kernel regression method to delineate facies. In preparation.***

Many methods for the interpolation of scattered data exist (Franke, 1982, and some of them have been used for geologic facies reconstruction (i.e. Ritzi et al., 1994, Guadagnini et al., 2004, Tartakovsky & Wohlberg 2004, Wohlberg et al., 2006, Tartakovsky et al., 2007). In particular, Tartakovsky et al. (2007) compared the fractional error obtained in two synthetic examples using three approaches: indicator kriging (IK) (Isaaks & Srivastava, 1990, Ritzi et al., 1994, Guadagnini et al., 2004), support vector machines (SVM) (Tartakovsky & Wohlberg 2004, Wohlberg et al., 2006) and nearest-neighbor classification (NNC) (Dixon, 2002). Different sampling densities were used for comparison, ranging from 0.28% to 3.06% and located randomly, following a 2D Poisson random process. Here sampling density refers to the proportion of pixels where hard data is available (classified pixels). Their analysis indicated that NNC outperformed IK in terms of reconstruction error in both examples and SVM slightly outperformed NNC in one of the examples.

There exist a number of reconstruction methods available in different disciplines that to our knowledge have never been used in geological reconstruction. A potential reason for this is that these methods were devised for the presence of massive data sets that are never available in geological facies reconstruction. One family of methods is based on kernel regression functions, widely used in signal theory for solving different problems such as image denoising, upscaling, interpolation, fusion, etc. Such methods have proved to be efficient for problems such as restoration and enhancement of noisy and/or incomplete sampled images. While in general regression methods have been used for reconstruction of images from extensive data sets, in principle there is no reason not to

use them when information is sparse. As an example, Takeda et al. (2007) tested a kernel regression method on an image reconstruction case in which only 15% of the pixels were present, obtaining a very good reconstruction of a 2D image.

Making an analogy between image reconstruction (from irregularly sampled data) and facies delineation (when scattered sampling points exist), we investigate the performance of the SKR method considering a different problem to that for what it was originally developed, having far less information available for the delineation (reconstruction). The aim is to give insight to the different tuning parameters in the method in order to get a range of potential values that can make the method useful for geological facies reconstruction, with emphasis in delineation of connectivity patterns.

This chapter is structured as follows; Section 3.2 briefly describes the fundamental concepts of facies reconstruction. Section 3.3 presents the details of the data-adapted kernel regression method. We test this method with respect to the NNC method in Section 3.4 by means of four synthetic images, here including the two figures profusely investigated by Tartakovsky et al. (2007).

3.2. THE CONCEPT OF FACIES RECONSTRUCTION

The term facies is used in geology to differentiate among geological units on the basis of interpretive or descriptive characteristics, such as conditions of formation, mineralogical composition, presence of fossils (biofacies), structures, grain size, etc.

(Tarbuck et al., 2002). In this work, we work with the consideration that each facies is a clear distinctive geology unit understood on the descriptive sense. Keeping this consideration in mind, facies reconstruction is defined as the process of assigning each unsampled point (eventually also the sampled ones if misclassification errors are admitted) to one facies. Formally, for any given facies F_k, the reconstruction problem can be addressed using an indicator function defined as

$$I(\mathbf{x}, F_k) = \begin{cases} 1 & \mathbf{x} \in F_k \\ 0 & otherwise \end{cases} \qquad \text{(Equation 3.1)}$$

where the indicator variable $I(\mathbf{x},F_k)$ is equal to 1 when a particular point in the domain, $\mathbf{x}$, can be classified as belonging to facies F_k and zero otherwise. In this work we assume that the available data from the sampling points are clearly distinctive in order to be unmistakenly classified as indicated in (Equation 3.1), without interpretation errors. From now on we consider that only two facies are used for geological mapping, but it could be easily extended to any finite number of facies by direct superposition. In such a case the problem can be posed as reconstructing only facies F_1.

Several methods have been proposed in the literature to estimate the spatial distribution of the indicator variable $I(\mathbf{x},F_1)$. Here we compile only three of such methods. The first one is indicator kriging (IK) (Journel, 1983), a method that provides a least-squares estimate of the probability that $\mathbf{x}$ belongs to F_1 conditioned to nearby data. Once a threshold value is given, a distinction between categories (facies) can be done. The method relies on the theory of random functions to model the uncertainty of not having data at unknown locations. It accounts for the inherent spatial correlation of data but typically fails to properly estimate curvilinear geological bodies. Multiple point

geostatistics (Strebelle, 2000) can overcome most of these problems by largely relying on an empirical multivariate distribution inferred from training images, i.e., under the assumption that significant information about the spatial distribution of facies is known from external sources (outcrops, modeling of sedimentological processes,…).

Alternatively, Support Vector Machine (SVM) methods are a set of popular tools for data mining tasks such as classification, regression, and novelty detection (Vapnik, 1963; Bennett and Campbell, 2000). SVM takes a training data, i.e., a set of n data points $J_i = J(\mathbf{x}_i, F_1) \in \{-1,1\}$, $i=1,..,n$, and separates them into two classes by delineating the hyperplane that has the largest distance to the nearest training data point of any class.

Last, the nearest-neighbor classification (NNC) simply classifies each point in the domain by finding the nearest (not necessarily in the Euclidean sense) training point, looking at the corresponding class for that training point and assigning it to the unsampled location.

A comparison of these three methods is provided in a recent series of papers by Tartakovsky and Wholberg (2004), Wholberg et al. (2006), and Tartakovsky et al. (2007). Surprisingly, the NNC method outperformed the more sophisticated ones, i.e., SVM and IK, indicating the validity of the parsimony principle for this problem. Yet, the comparison between methods in such works was done only in terms of the number of misclassified points, without considering other performance metrics such as

connectivity between facies that may have a strong relevance in the overall hydraulic behavior of an aquifer. We consider this issue as non-ideal and in the next section we seek for a method that can account for local anisotropy in the search directions to be able to discriminate the presence of elongated shapes.

3.3. NONPARAMETRIC REGRESSION APPROACH FOR FACIES CLASSIFICATION

3.3.1. NONPARAMETRIC REGRESSION MODELS

Suppose that we ignore the fact that the target classification output is a binary function $I(\mathbf{x},F_1)$. Instead, let us consider that it is a continuous function that depends on location (**x**) and on a number of (yet unknown) parameters $\mathbf{b}=[b_0,b_1,\ldots,b_N]^T$. The regression model for facies classification assumes that the measured data $I_i=I(\mathbf{x}_i,F_1)$, $i=1,\ldots,n$, can be expressed as

$$I_i = m(\mathbf{x}_i;\mathbf{b}) + \varepsilon_i, \qquad i = 1,..,n, \qquad \text{(Equation 3.2)}$$

where $m(\mathbf{x}_i,\mathbf{b})$ is the regression function to be determined, and ε_i are independent and identically distributed zero mean noise values. Nonparametric regression is a form of regression analysis in which the function m is exclusively dictated by the data. At each point **x** the conditional expected value of the dependent variable (the indicator variable) can be estimated, i.e., $m(\mathbf{x},\mathbf{b})=\mathrm{E}[I(\mathbf{x},F_1)]$. The interest of nonparametric regression to facies reconstruction resides on the fact that the conditional expected value of the indicator variable is exactly the probability that the given facies F_1 prevails at that location, since

$$E\{I(\mathbf{x},F_1)\} = 1\cdot \text{Prob}\{\mathbf{x}\in F_1\} + 0\cdot \text{Prob}\{\mathbf{x}\notin F_1\} = \text{Prob}\{\mathbf{x}\in F_1\} \quad \text{(Equation 3.3)}$$

By definition, the probability of occurrence of a given facies is a continuous variable ranging between 0 and 1. In order to separate the data into classes or facies we must then establish a cut-off in the estimate of the indicator variable. This is similar to the facies reconstruction problem posed by the geostatistical indicator kriging approach. In this case, Ritzi et al. (1994) has suggested to define the boundary between facies by the isoline Prob$\{\mathbf{x}\in F_k\}$=p_k, where p_k is estimated as either the global mean of the indicator values or the empirical relative volumetric fraction of the facies F_k. We propose here to use the same approach for classifying facies with regression methods. The benefits of such approach will be explored in section 3.4.

Two kernel regression methods, namely the classical (CKR) and the adaptive steering (SKR) are presented next, and later their performance is compared in a number of synthetic cases.

3.3.2. CLASSICAL KERNEL REGRESSION (CKR)

Let us consider a local Taylor expansion of the mean response $m(\mathbf{x},\mathbf{b})$ of the indicator values around the estimation location $\mathbf{x}_0$,

$$m(\mathbf{x};\mathbf{b}) \approx m(\mathbf{x};\mathbf{b},\mathbf{x}_0) = b_0 + b_1x' + b_2y' + b_3z' + b_4x'^2 + b_5x'y' + b_6y'^2 + b_7x'z' \ldots \quad \text{(Equation 3.4)}$$

where $\mathbf{x}'=\mathbf{x}-\mathbf{x}_0$ is the distance from the estimation location, b_0 is the mean response at $\mathbf{x}_0$, $[b_1,b_2,b_3]^T$ is the gradient of the mean response at $\mathbf{x}_0$, and so on. The order of the polynomial is in principle arbitrary. Nonparametric regression generalizes the standard

regression approach by locally estimating **b** at a given location $\mathbf{x}_0$ with only nearby data. This is done by weighting data located far away from the estimation location with a kernel function K_H defined as

$$K_H(\mathbf{x}) = \frac{1}{\det(\mathbf{H})} K\left(\mathbf{H}^{-1}\mathbf{x}\right) \qquad \text{(Equation 3.5)}$$

where **H** is a matrix that controls the degree of smoothing and is user dependent. Section 3.4 will explore the choice of kernel parameters for optimal facies reconstruction.

The kernel function K is a continuous, bounded, and symmetric real function centered at zero that integrates to one and typically decays with distance. The choice of the kernel is known not to significantly affect the final solution and therefore a standard Gaussian distribution is typically used for mathematical convenience. In n dimensions this is written as

$$K(\mathbf{x}) = \frac{1}{(2\pi)^{n/2}} \exp\left[\frac{1}{2}\mathbf{x}^T\mathbf{x}\right] \qquad \text{(Equation 3.6)}$$

For any given estimation location $\mathbf{x}_0$, the principle of least squares expresses that one should choose as estimates of **b** those values that minimize the weighted sum of squared residuals, S(**b**), the residual being the difference between data values and model predictions,

$$S(\mathbf{b}) = \sum_{i=1}^{n} \left[I_i - m(\mathbf{x}_i; \mathbf{b}, \mathbf{x}_0)\right]^2 K_H(\mathbf{x}_i - \mathbf{x}_0) \qquad \text{(Equation 3.7)}$$

Let us express equation (Equation 3.2) in matrix form,

$$\mathbf{I} = \mathbf{Xb} + \mathbf{e} \qquad \text{(Equation 3.8)}$$

where $\mathbf{I}=[I_1,..,I_n]^T$, $\mathbf{e}=[\varepsilon_1, \ldots,\varepsilon_n]^T$, and $\mathbf{X}$ is a matrix composed of n rows and a number of columns that is associated with the degree of the polynomial chosen for **b** (i.e., in 3-D would be 4 for order 1, 10 for order 2,…)

$$\mathbf{X}=\begin{bmatrix} 1 & x_1' & y_1' & z_1' & x_1'^2 & x_1'y_1' & y_1'^2 & x_1'z_1' & \ldots \\ \ldots & & \ldots & & \ldots & & & \ldots & \\ 1 & x_n' & y_n' & z_n' & x_n'^2 & x_n'y_n' & y_n'^2 & x_n'z_n' & \ldots \end{bmatrix} \qquad \text{(Equation 3.9)}$$

Then, the optimization problem is written as

$$\min_{\mathbf{b}} S(\mathbf{b}) = \min_{\mathbf{b}} \left(\mathbf{I}-\mathbf{Xb}\right)^T \mathbf{W}\left(\mathbf{I}-\mathbf{Xb}\right) \qquad \text{(Equation 3.10)}$$

where **W** is a diagonal weight matrix given by

$$\mathbf{W} = \mathrm{diag}\left\{K_H(\mathbf{x}_1-\mathbf{x}_0),...,K_H(\mathbf{x}_n-\mathbf{x}_0)\right\} \qquad \text{(Equation 3.11)}$$

Setting $\partial S(\mathbf{b})/\partial b_j=0$ to each parameter b_j we obtain the following solution

$$\hat{\mathbf{b}} = \left(\mathbf{X}^T\mathbf{WX}\right)^{-1}\mathbf{X}^T\mathbf{WI} \qquad \text{(Equation 3.12)}$$

This solution is formally the same to that of standard regression but the matrices **W** and **X** depend now on the estimation location $\mathbf{x}_0$. Knowing the optimal estimate of **b**, the probability that **x** belongs to F_1 can be estimated by

$$\mathrm{Prob}\left\{\mathbf{x}\in F_1\right\} = E\left\{I(\mathbf{x},F_1)\middle|\mathbf{x}\right\} = m(\mathbf{x}_0,F_1,\mathbf{x}_0) = \hat{b}_0 \qquad \text{(Equation 3.13)}$$

Let us define $\mathbf{W}_{eq}$ by

$$\mathbf{W}_{eq} = \mathbf{e}_1^T\left(\mathbf{X}^T\mathbf{WX}\right)^{-1}\mathbf{X}^T\mathbf{W} \qquad \text{(Equation 3.14)}$$

where $\mathbf{e}_1$ is a column vector with first element equal to one, and the rest equal to zero. Then, the Classical Kernel Regression (CKR) algorithm can be seen as a local weighted averaging of the data in which the probability that $\mathbf{x}$ belongs to F_1 is determined by the following linear interpolation of indicator values

$$\hat{b}_0 = \mathbf{W}_{eq}^T \cdot \mathbf{I} \qquad \text{(Equation 3.15)}$$

Hence, $\mathbf{W}_{eq}$ are actually the equivalent weights of the indicator data values. The forms of these equivalent weights are exclusively dictated by the polynomial order chosen in (Equation 3.4).

3.3.3. STEERING KERNEL REGRESSION

The SKR method comes as a direct extension of the CKR algorithm. Since the latter is nothing but a weighted average of indicator data values, the final regression estimate of Prob$\{\mathbf{x}\in F_1\}$ only depends on the geometric configuration of the data, and therefore ignores the inherent correlations between data positions and their values. Takeda et al. (2007) developed a SKR algorithm to include key structural features into the estimated fields.

The key idea behind the SKR algorithm is to modify the size and orientation of the regression kernel to assign more weight along the direction of highest local spatial correlation. The advantage of doing this to classify facies is the following: consider a point $\mathbf{x}_0\in F_1$ located close to a facies boundary; the conventional CKR algorithm

(symmetric spherical kernel) will estimate the probability that $\mathbf{x}_0$ belongs to F_1 by equally considering both nearby samples of the same facies F_1 and samples of other facies located beyond the boundaries. The SKR method is designed to adapt the regression kernel to the boundary isosurface so as to assign more weight to those samples belonging to the same facies. This way, the denoising is affected most strongly along the boundaries, rather than across them, resulting in a strong preservation of details in the final output.

The algorithm works by reorienting the smoothing matrix in the direction of the gradients of the mean response m(**x**,**b**) through a redefinition of the kernel matrix

$$\mathbf{H}_i^{steer} = h\mathbf{C}_i^{-1/2} \qquad \text{(Equation 3.16)}$$

$$\mathbf{C}_i \approx \left(\overline{\nabla m(\mathbf{x}_j, \hat{\mathbf{b}}) \cdot \nabla^T m(\mathbf{x}_j, \hat{\mathbf{b}})}\right), \qquad \mathbf{x}_j \in w_i \qquad \text{(Equation 3.17)}$$

where the overbar stands for averaging over the mean response adjacent to $\mathbf{x}_i$, w_i is the window search around $\mathbf{x}_i$, and h is a global smoothing parameter.

In contrast to the CKR algorithm, the smoothing matrix $\mathbf{H}^{steer}$ at each individual point $\mathbf{x}_i$ depends now on the solution of the regression function m(**x**,F_1). This makes the SKR method to be nonlinear in nature. Its application must be therefore iterative, starting with a first initial estimate of m(**x**,F_1) computed, for instance, with the CKR method. This estimate is used to measure the dominant orientation of the local gradients, then used to sequentially steer the local kernel through (Equation 3.17), resulting in elongated, ellipsoidal contours spread along the indicator isosurface (isocurve in 2D).

We must state that while the method is applicable to 3D reconstruction problems, here we present the details only for the 2D problems. The main reason is to be able to use the same synthetic examples available in the literature for geologic facies reconstruction using IK, SVM or NNC methods. Under these conditions, and from (Equation 3.16), the new form of the regression kernel is

$$K_{H_i^{steer}}(\mathbf{x}_i - \mathbf{x}_0) = \frac{\sqrt{\det(\mathbf{C}_i)}}{2\pi h} \exp\left[\frac{(\mathbf{x}_i - \mathbf{x}_0)^T \mathbf{C}_i (\mathbf{x}_i - \mathbf{x}_0)}{2h^2}\right] \qquad \text{(Equation 3.18)}$$

When estimating the covariance matrix $\mathbf{C}_i$ through (Equation 3.17), the resulting matrix can be rank deficient and unstable. To overcome this problem, a multiscale technique for estimating local gradients (Takeda et al., 2007) can be adopted. Let us consider the following matrix $\mathbf{G}_i$ formed by a collection of p estimated gradient vectors at the neighborhood of the sampled location $\mathbf{x}_i$

$$\mathbf{G}_i = \begin{bmatrix} \nabla m(\mathbf{x}_1, \mathbf{b}) \\ \dots \\ \nabla m(\mathbf{x}_p, \mathbf{b}) \end{bmatrix}, \quad \mathbf{x}_j \in w_i, \quad j = 1,\dots,p \qquad \text{(Equation 3.19)}$$

The singular value decomposition of $\mathbf{G}_i$ factorizes this matrix in the following form

$$\mathbf{G}_i = \mathbf{U}_i \mathbf{S}_i \mathbf{V}_i \qquad \text{(Equation 3.20)}$$

where the diagonal entries S_{jj} of $\mathbf{S}_i$ (singular values) represent the energy in the dominant directions (singular vectors) of the local gradient field. These dominant directions are given by the column vectors of the matrix $\mathbf{V}_i$. In particular, the second column of $\mathbf{V}_i$, $[V_{12}, V_{22}]^T$, determines the direction of smallest energy and represents the dominant orientation angle of $\mathbf{C}_i$ (direction with highest local spatial correlation) by

$$\theta_i = \arctan\left(\frac{V_{12}}{V_{22}}\right) \qquad \text{(Equation 3.21)}$$

The actual shape of the regression kernel is then calculated from the energy associated with the dominant gradient directions,

$$E_{\max} = \frac{S_{11} + \lambda_1}{S_{22} + \lambda_1}, \qquad E_{\min} = \frac{S_{22} + \lambda_1}{S_{11} + \lambda_1} \qquad \text{(Equation 3.22)}$$

where λ_1 is a regularization parameter that dampens the effect of noise and restricts the ratio from becoming degenerate. Knowing these parameters, the covariance matrix can be calculated by the a combination of a scaling parameter γ_i, a rotation matrix $\mathbf{R}_i$, and an elongation matrix $\mathbf{E}_i$ by means of

$$\mathbf{C}_i = \gamma_i \mathbf{R}_i \mathbf{E}_i \mathbf{R}_i^T \qquad \text{(Equation 3.23)}$$

The different terms in (Equation 3.23) are defined as

$$\mathbf{R}_i = \begin{bmatrix} \cos\theta_i & \sin\theta_i \\ -\sin\theta_i & \cos\theta_i \end{bmatrix} \qquad \text{(Equation 3.24)}$$

$$\mathbf{E}_i = \begin{bmatrix} E_{\max} & 0 \\ 0 & E_{\min} \end{bmatrix} \qquad \text{(Equation 3.25)}$$

$$\gamma_i = \left(\frac{S_{11}S_{22} + \lambda_2}{M}\right)^{\alpha}, \qquad \text{(Equation 3.26)}$$

where λ_2 is another regularization parameter aimed at dampening the effect of the noise and keeping the scaling parameter from becoming zero, α is a structure sensitive parameter satisfying that $0<\alpha<1$, and M is the number of samples in the local analysis window w_i.

3.3.4. UNCERTAINTY IN FACIES CLASSIFICATION

At this stage, it is important to highlight the following advantage of the SKR method compared to deterministic algorithms, e.g., the nearest neighbor classification (NNC). Statistical approaches not only provide a map of the spatial distribution of the estimates of indicator values (i.e., the probability that a given point belongs to a facies), but also the error variance of the estimates of **b**. If the error terms ε_i are uncorrelated, and all have the same variance σ^2, then it can be shown that the estimator (Equation 3.12) is an unbiased estimate of **b**, and that the variance-covariance of the estimation matrix is

$$\mathbf{C}_b = \sigma^2 \left(\mathbf{X}^T \mathbf{W} \mathbf{X} \right)^{-1} \qquad \text{(Equation 3.27)}$$

Thus, the variance of the estimate of Prob$\{\mathbf{x} \in F_1\}$ can be determined by

$$\sigma^2_{SKR} = \sigma^2 \mathbf{e}_1 \left(\mathbf{X}^T \mathbf{W} \mathbf{X} \right)^{-1} \mathbf{e}_1^T \qquad \text{(Equation 3.28)}$$

And the error variance can be estimated as

$$\sigma^2 \approx s^2 = \frac{S(\hat{\mathbf{b}})}{n - N} \qquad \text{(Equation 3.29)}$$

Where N is the number of estimated parameters. Knowing this, one can define an approximate confidence region in which the border between facies is most expected to be found. This will be explored in section 3.4.

3.4. SYNTHETIC EXAMPLES

3.4.1. METHODOLOGY

Since the NNC has been already demonstrated to outperform SVM and IK approaches (Tartakovsky et al., 2007), in this section we only compare the performance of the SKR method with the NNC. The NNC algorithm is provided in the Appendix for completeness. Four synthetic geological field settings formed with two distinct facies (see Figure 3-1) were used to test the SKR method and compared its performance with the NNC. Two of these fields, Figures 1a and 1b, are identical to the ones presented by Tartakovsky et al. (2007); the remaining two were specifically generated for this work. Figure 3-1c is a curvilinear shape, obtained from an abandoned meander in the Ebro river (Spain), potentially indicating the shapes of paleochannels that could be found in the subsurface. Figure 3-1d is just a circle, in order to test the performance of the algorithm for a very simple shape. Each of the figures consists of an image data discretized in 60×60 (=3600) pixels. Red and blue pixels correspond to facies F_1 and F_2, respectively. In accordance to previous sections, the following indicator function is used for facies reconstruction purposes,

$$I(\mathbf{x}, F_1) = \begin{cases} 1 & \mathbf{x} \in F_1 \\ 0 & \mathbf{x} \in F_2 \end{cases} \qquad \text{(Equation 3.30)}$$

The objective of the numerical simulations is to reconstruct the facies depicted in each individual image from a few measurements. We consider a random data set consisting of 10, 20, 30, 50, 80, and 110 measurements, and corresponding to a range of 0.28% to 3.06% of the total pixels investigated. Emphasis is given to sample densities between 10 and 30, which illustrate the most typical problem encountered in subsurface hydrology,

i.e., those with scarce information covering a very low portion of the simulation domain. The SKR is used with a quadratic polynomial approximation of the mean response $m(\mathbf{x},F_1)$ in (Equation 3.4) and a Gaussian kernel.

An analysis of the fractional error of the reconstructed images is used to compare the performance of the SKR method with that of NNC. For each realization, the fractional error was obtained as the ratio of misclassified to the total number of pixels in the images. One hundred realizations were created for each sample density, and the fractional error reported is the average over the ensemble of realizations. For comparison purposes, selected points associated with each sample density were the same for the SKR and the NNC methods. It is important to notice that Tartakovsky et al. (2007) used only 20 (rather than 100) randomly generated realizations for each sample density; for this reason, our calculated fractional error for NNC, although similar, is slightly different to theirs.

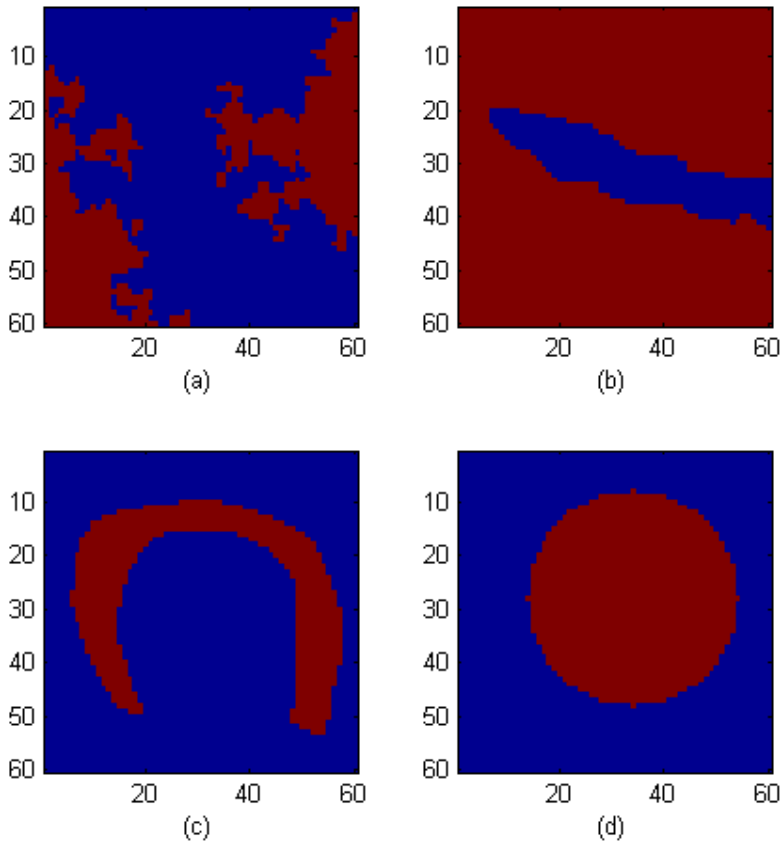

Figure 3-1. Synthetic fields used for facies delineation: a and b are the same figures presented by Tartakovsky et al. (2007). We generated Figure 3-1 (c) and (d) considering a real case scenario (a meander from the Ebro river, Spain, and a circle a simple geometric figure). Gray and black colors indicate the two facies.

The SKR method provides the probability of occurrence of facies F_1 at a given location. Therefore, the output data is a continuous variable (i.e., $m(\mathbf{x},\mathbf{b}) \in [0,1]$). A cut-off in the estimated values is then necessary to classify the data into facies. We explore two different strategies to introduce this cut-off. The first strategy considers that no *prior*

information on the relative volumetric proportion of facies is known. In this case, the boundary between facies is determined by the isoline $\text{Prob}\{\mathbf{x}\in F_1\}=\text{Prob}\{\mathbf{x}\in F_2\}=0.5$, expressing that both facies have the same probability of existence at the facies boundaries. We denote this method as SKR(0). When prior information on the relative volumetric proportion of facies is known, then one can defined the boundary between facies by the isoline $\text{Prob}\{\mathbf{x}\in F_1\}=p_1$ (i.e., $\text{Prob}\{\mathbf{x}\in F_2\}=1- p_1$), where p_1 is estimated either by the global mean of the indicator values or the empirical relative volumetric fraction of facies F_1. The latter method is similar to the facies reconstruction problem posed by the geostatistical indicator kriging approach proposed by Ritzi et al. (1994). We will refer to this strategy as SKR(%).

3.4.2. CHOOSING THE KERNEL PARAMETERS

Five different parameters control the solution of the SKR method: (1) the global smoothing parameter h, equation (Equation 3.16); (2) the size of the local orientation analysis window w, equation (Equation 3.17); (3) the regularization parameter λ_1, equation (Equation 3.22); (4) the structure sensitive parameter α, equation (Equation 3.26); and (5) a second regularization parameter λ_2. This last one is directly fixed to 10^{-7}. A sensitivity analysis of the lowest fractional error was carried for the remaining four parameters.

Figure 3-2 provides a series of contour plots of the lowest fractional error associated with the image shown in Figure 3-1a and only for the case of lowest sample density (10

data points). Each contour plot displays the lowest fractional error as a function of two parameters. Blue dots correspond to the estimated values used to generate the contour plots. In general, the lowest fractional error is mainly controlled by h and α, being the output solution quite insensitive to w and λ_1. A good quality of facies classification reconstruction is typically obtained with h=1 (pixel), w=5 (pixel), λ_1=500 and α=0.01.

This optimum combination of parameter values is explained as follows: The structure sensitivity parameter α, which must satisfy the condition $0<\alpha<1$, is devised to increase the steering kernel area in regions where large fluctuations exist (high-frequency data), so that large α values are able to produce smooth estimates in those high-frequency data regions. The reconstruction problem in hydrogeology typically involves small densities and low-frequency data (scarce data) and thereby this correction is somehow uncalled for. Accordingly, the sensitivity analysis yields α=0.01, which basically expresses that the scaling factor γ_i is always close to 1.

The window size w defines the search area over which the gradients ∇m used to determine the local covariance function $\mathbf{C}_i$ at a data point location are estimated. Results show that a relatively small region (w=5 pixels) is sufficient to properly capture the patterns of $\mathbf{C}_i$, which is most likely due to the use of a small sample population and the lack of noise in the data values.

The parameter λ_1 is a regularization parameter used to avoid numerical singularities during the estimation of the principal components of the elongation matrix $\mathbf{E}$. Results show that the lowest fractional error decays with increasing λ_1. Large values are needed

here because S_{11} and S_{22} in equation (Equation 3.21) are relatively large for the field conditions considered.

Given that scaling is not required ($\gamma_i \approx 1$) and that the solution is not much sensitive to both w and λ_1, the global smoothing parameter h appears as the main controlling factor. This parameter determines the area underneath the steering kernel so that large h values will increase the influence of distant data points to the final estimation. Results show that a small h value close to 1 pixel is required in this synthetic example, which implies small steering kernel areas.

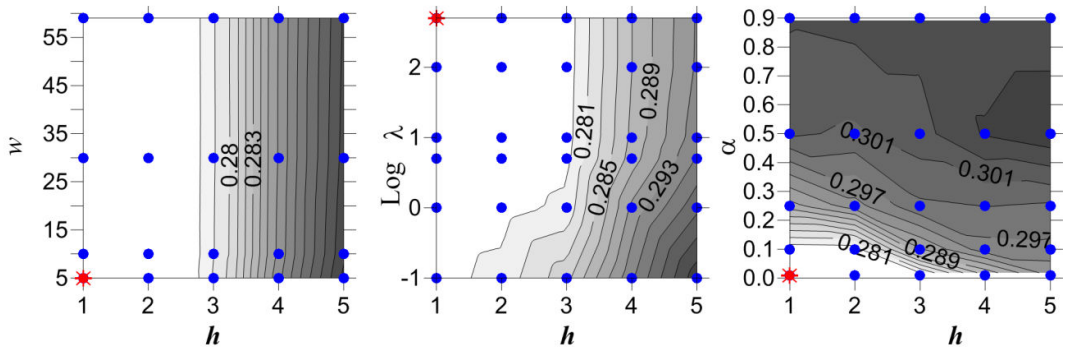

Figure 3-2. Sensitivity analysis for the four fix parameters during size of the local orientation analysis window (w), the regularization for the elongation parameter (λ), the structure sensitive parameter (α) and the global smoothing parameter (h). Blue dots indicate the different value choices for the calculation of the fractional errors and the red star indicates the value used for our calculations, coincidently with the lowest fractional error.

An illustration of the shape of the steering kernel ellipses obtained during the iterative solution of the SKR method is shown in Figure 3-3 for a sample density of 0.83% (i.e., 30 data points). Figure 3-3a shows the reference image, whereas the series of Figures (b)-(e) display the reconstruction solution at different iterations. Initially, there is no information on the local correlation of data values (gradients) and therefore the ellipses are (uninformative) circles of radius close to 1 pixel. In subsequent iterations, a better gradient estimation is increasingly achieved and circles are reshaped to ellipses elongated in the direction of the highest local correlation (smallest gradient). As a result, large weights are given to the data values located in the direction of the local highest correlation while other data points are practically ignored. Based on this observation, the application of the SKR method to facies reconstruction can be seen as a specialized nearest neighbor procedure in which the distance metric is not measured by an Euclidian distance but in terms of the highest local correlation, changing for each data location.

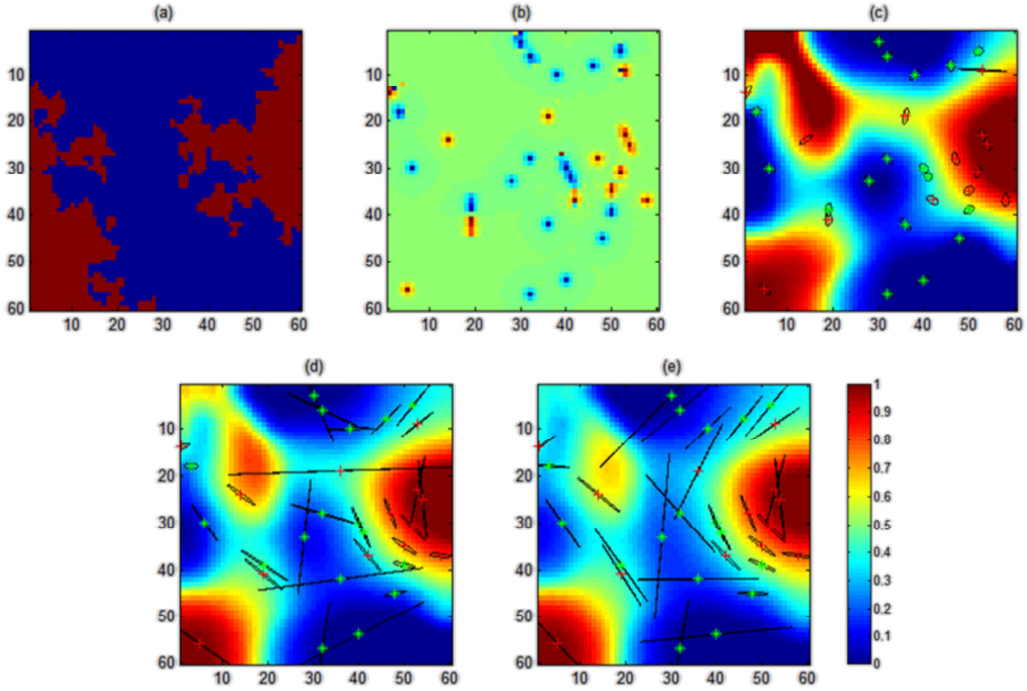

Figure 3-3. Iteration comparison. a) Original figure, corresponding to Figure 3-1(a). In all this set, random sampling points are shown as blue and red squares, for this example a sample density of 30 is shown. b) Classical Kernel Regression result after interpolation. First, second and third iterations of the Steering Kernel are shown in c), d) and e), respectively.

The parameter sensitivity analysis presented here considers a given sample density and a particular image. To complete the analysis, Figure 3-4 presents the global smoothing parameter *h* as a function of sample density and varying for each reference image. For a given sample density, the *h* value provided is the best estimate obtained manually by trial-and-error to minimize the fractional error. Figure 3-4 shows that, in the lowest sampling density, which is the typical scenario in subsurface hydrology, the lowest fractional error is always achieved when h=1 for both methods, i.e., the SKR(0) and the SKR(%). A generalization is harder to state for other sampling densities and reference

images. Nevertheless, it can be observed from Figures 1a and 1d that higher values are required for sampling densities between 30 and 80.

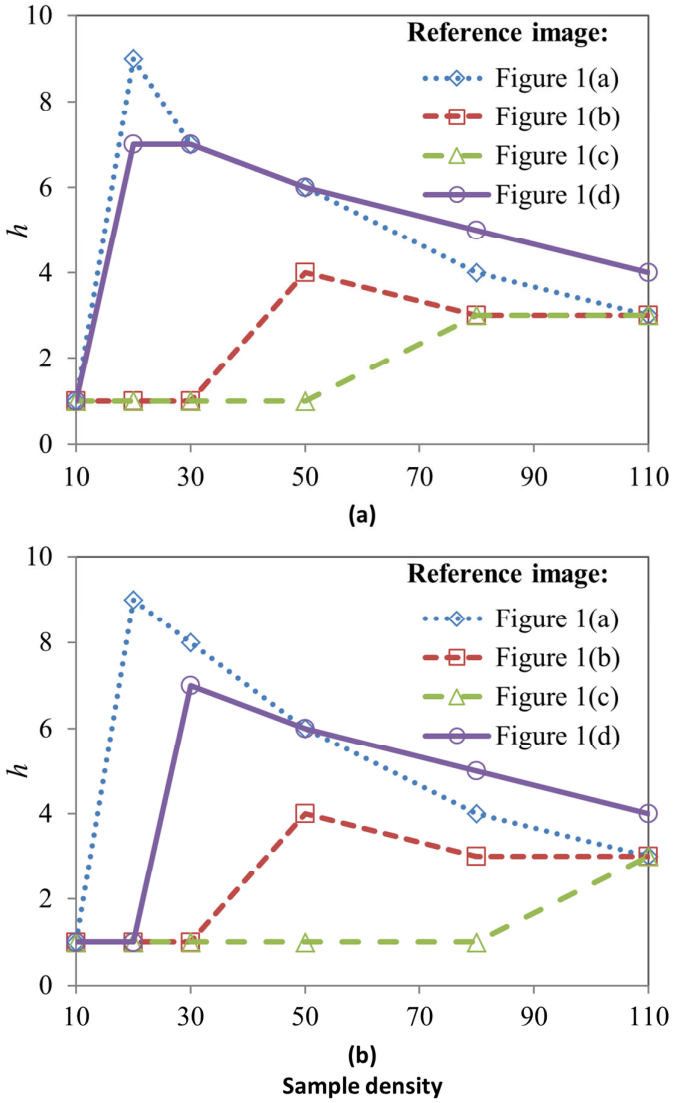

Figure 3-4. Optimal global smoothing parameter (h_b) comparison for the steering kernel regression function for the two SKR conditions: a) SKR(0) and b) SKR(%). Values on the corners of the chart indicate the sample density, while the interior axis represents the h_b value. On this graph it is clear that for the lowest sample density (10 samples) a low h_b value is the optimal, while for the highest sample density an intermediate value (3-4)

is ideal; for the other sample densities this parameter value varies between figures, with generally high values (above 5) for Figure 3-1 (a) and (d) on both conditions.

Along the same lines, Figure 3-5 shows the fractional error obtained as a function of *h* for the four images analyzed and different sample densities considered. Other parameters were set to *w*=5 pixels, λ_1=500 and α=0.01. Results show that, in most cases, the SKR(0) method with no prior information on the volumetric proportion of facies yields larger fractional errors compared to the SKR(%) method. This effect is significantly visible for small sample densities, which is the typical scenario in real applications. Moreover, the fractional error tends to increase with *h*, a fact that is especially evident for Figures 3-5b and 3-5c.

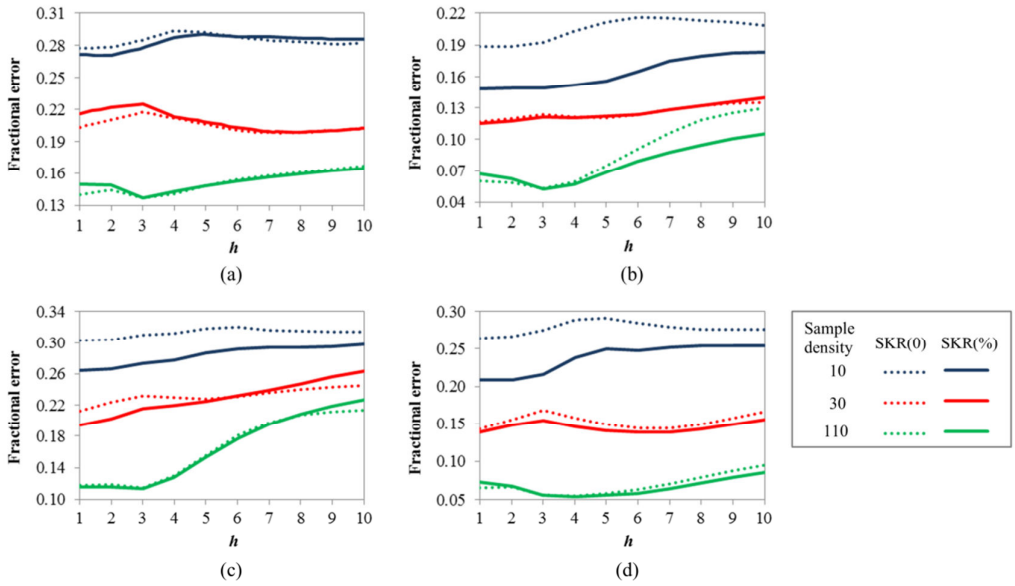

Figure 3-5. Fractional error variation vs. *h* for the four figures analyzed, here they are presented in the same order as shown in Figure 3-1: a) Figure A, b) Figure B, c) Meander, d) Ball. Discontinuous and continuous lines represent respectively the fractional error when SKR(0) and SKR(%) are considered.

3.4.3. SIMULATION RESULTS

Figure 3-6 shows the fractional error as a function of sample density for the different methods employed. In all cases, the fractional errors associated with both the SKR(0) and the SKR(%) methods are smaller than that of the NNC. Interestingly, while the performance of the SKR(0) method is only slightly better than that of the NNC method, with a relative error difference no larger than 1% in most cases, the introduction of prior information into the analysis via the SKR(%) method is capable of significantly outperform the other two approaches. This impact is most noticeable in Figure 3-1c. It is important to highlight here that for all the evaluated images, the benefit (in relative terms) given by the SKR(%) method is higher for the smaller sampling densities. This is an important finding in itself. Under real circumstances, in typical hydrogeology problems it is very likely that the number of data points will be rather limited, and as so, the SKR(%) method constitutes a valuable instrument to interpret facies delineation with the lowest estimation error.

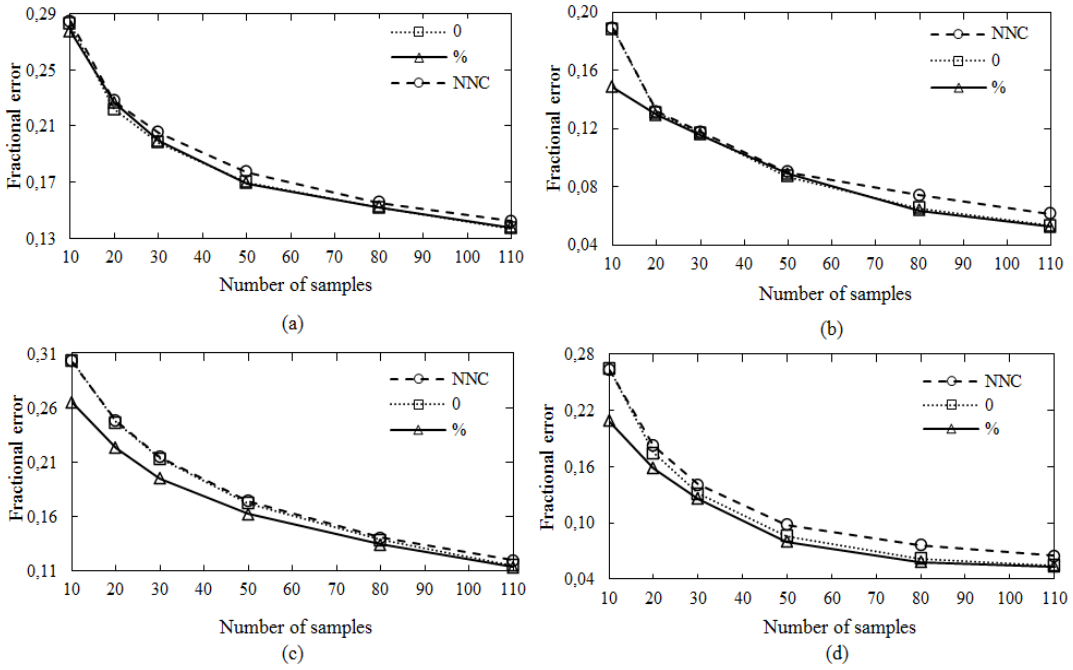

Figure 3-6. Fractional error comparison. From top to bottom synthetic fields (a), (b), (c) and (d) as indicated in Figure 3-1. NNC stands for nearest neighbor classification, 0 for SKR(0) and % for SKR(%).

Let us emphasize the real benefit of using SKR(%) compared to the NNC algorithm. Consider the problem of reconstructing the image shown in Figure 3-1a from only 30 data points randomly located. Figure 3-7 compares the true image (cross symbols represent the sampling points) with the output of NNC and 4 iterations of the SKR(%) method. In this case, the fractional error associated with the SKR(%) method is only slightly better than that of the NNC but still important reconstruction features can be distinguished. NNC only depends on data configuration and not on the actual values or their spatial correlation. As such, its reconstructed image (Figure 3-7b) fails to represent the central spatial continuity observed in facies F_1, clearly extending from the northern to the southern boundaries. Instead, with only four iterations, the SKR(%) is able to

correctly identify this spatial continuity of data values and properly represent the true connection north-south.

Figure 3-3 illustrates the evolution of the local kernel functions associated to each data point in the same problem. In these images, the variable represented is the direct output data given by the SKR method without applying a classification strategy. We observe the progressive increase in the ratio of the two axes of the ellipse.

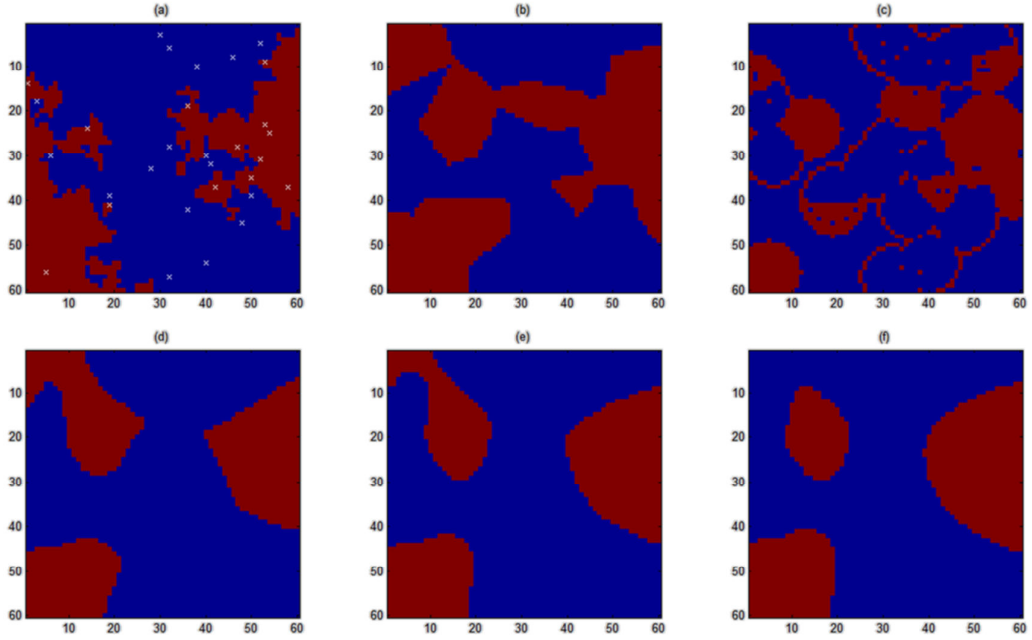

Figure 3-7. (a) Original figure, showing the location of the random samples considered (b) Nearest-neighbor classification, (c) Classic kernel regression h_a=1. Second order steering kernel regression: (d) iteration 1, (e) iteration 2, (f) iteration 3. Figures c, d, e and f are the result of equation 3.30.

In addition to the recognition of spatial continuity, the SKR(%) is also capable of providing a measure of uncertainty in the delineation of the facies boundary. In

principle this is not possible for a deterministic approach, such as that of the NNC algorithm. Figure 3-8 presents different maps to evaluate the uncertainty in the estimation corresponding to the same example already used previously. Interestingly, there is a very good correlation between low variance and high sampling density areas and viceversa. From this map, one can also delineate a safe zone for drawing the border between facies, plotted as gray areas in Figure 3-8e, those corresponding to values above 0.3 times the standard deviation. By visual inspection, one can appreciate a very good agreement between the results from the SKR(%) method (Figure 3-8e) and the original facies boundaries visible in Figure 3-8a.

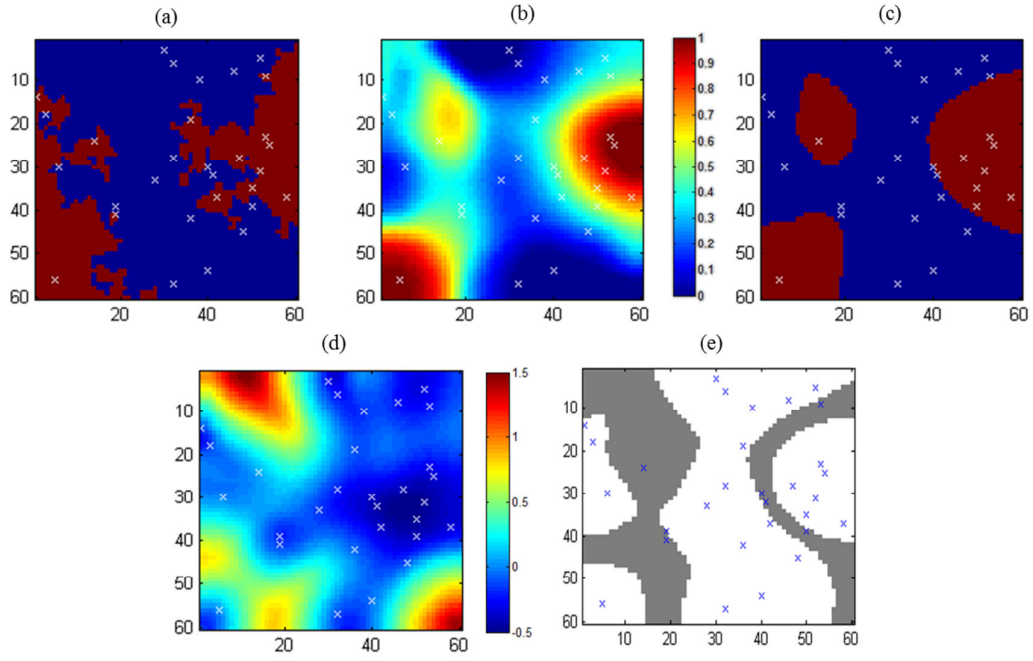

Figure 3-8. (a) Original figure, (b) steering kernel iteration 3, (c) steering kernel iteration 3 after equation 3.30, (d) Variance map showing the areas with the highest and lowest uncertainty (red and blue zones), (e) standard deviation map, showing in gray the area where the border between facies is more likely located.

3.5. CONCLUSIONS

A non-parametric method, SKR, originally designed for image processing (Takeda et al. 2007), has been presented and tested for its application as a facies delineation algorithm. The performance of the method was compared with the nearest neighbor classification, a method that has proven to be more efficient than others discussed in the literature (Tartakovsky et al., 2007). Four synthetic scenarios were used for the comparison: two of them identical to the figures presented by Tartakovsky et al. (2007), and the other two figures are new for this work, one inspired on a cartographied river meander, and the other being a representation of a simple geometry, a circle. For each example different tests were studied ranging from very sparse to sparse number of data points available.

Two variations of the SKR method were tested depending on whether additional information about the exact proportion of facies was introduced in the algorithm (SKR(%)) or not (SKR(0)).

Our results indicate that the SKR(0) method had similar or lower fractional errors than those obtained with NNC, except for two cases (Figure 3-1(c) and (d), with a sampling density of 0.28%). The SKR(%) outperformed all methods, with improvements up to 5% in misclassified points. The improvement is better in relative terms for lowest

sampling densities. This finding leads us to believe that the SKR(%) method would be an useful tool on real cases, when scattered and few sampling data points are expected.

One of the major advantages of the SKR method is the quantification of the uncertainty in the delineation of the facies boundaries. In this context, we presented a method to stochastically generate variance maps that allows one to identify potential areas where a boundary between facies is more likely to exist. An example of application for one of the study cases is provided showing the area over which there is most probably a boundary between facies.

4. INFILTRATION RATE VARIATIONS DUE TO TEMPERATURE FLUCTUATION IN AN ARTIFICIAL RECHARGE POND[3]

4.1. INTRODUCTION

Daily water temperature fluctuation is a common phenomenon that can be observed in surface water bodies exposed to environmental temperature changes; generally, natural water temperature variations can be of two types, seasonal variations (an annual cycle of low temperature during the winter and higher temperature during the summer) or daily fluctuations (higher temperatures during day light and lower temperature at night).

The impact of temperature variations in recharge has been assessed in a number of natural and artificial water bodies (Constanz et al., 1994; Constanz, 1998, Ronan et al., 1998, Lin et al., 2003, Braga et al., 2007). Temperature directly affects hydraulic conductivity, K, as shown in Equation 4.1:

$$K = k\left(\frac{\rho g}{\mu}\right) \quad \text{Equation 4.1}$$

[3] ***This chapter is based on the paper: Barahona-Palomo, M., Sanchez-Vila, X., Fernàndez-Garcia, D., Bolster, D., Pedretti, D., and Barbieri, M. 2014, Infiltration Rate Variations due to Temperature Fluctuation in an Artificial Recharge Pond. In preparation.***

Where k is the intrinsic permeability, g is the acceleration of gravity, ρ and μ are the density and viscosity of water, respectively; the latter two terms are temperature dependent.

Rorabaugh (1963) observed that streambed percolation rates from a river in Kentucky, USA were directly affected by seasonal changes in stream temperature. This author demonstrated that the seasonal increases in percolation losses during the summer were entirely predicted by the expected influence of temperature on the hydraulic conductivity K of the streambed. The magnitude of K is strongly temperature sensitive as a result of the strong temperature sensitivity of the viscosity of water (Muskat, 1937). As a consequence, a temperature increase from 0º to 25ºC in porous materials results in a doubling of the ponded infiltration rate (Constantz & Murphy, 1991).

During a 5 years study, Rorabaugh (1963) found that infiltration rates were comparable in winter and summer even though the stage was generally 10 times higher in winter. In another study, infiltration rates were higher in the late afternoon, when stream temperature is greatest, and lower in early morning, when stream temperature was lower (Ronan et al., 1998; Constantz, 1998; Braga et al., 2007).

Viscosity of water changes by approximately 2%/ºC between the temperature range of 15-35ºC and this change is suggested to lead to an estimated 40% change of infiltration rate between the summer and winter months (Lin et al., 2003). According to Iwata et al.

(1995), the value of K at a water temperature of 35ºC is twice that of a temperature of 7ºC.

Correction for temperature fluctuations are rarely considered during field measurements even though this effect might be a potential source of error (McKenzie & Cresswell, 2002).

After an extensive bibliographic research, it is our understanding that daily temperature variations in Artificial Recharge ponds have not been modeled and compared with field data, as a parameter that can manage the infiltration rate in highly permeable soils. In this chapter we study detailed recharge measurements in an artificial recharge basin in order to assess the impact of temperature variations in a temperate Mediterranean climate.

4.2. MATERIALS AND METHODS

4.2.1. STUDY SITE DESCRIPTION

The study site is located close to Barcelona, Spain (Figure 4-1). The facility includes two ponds that were constructed for artificial recharge experimentation. Infiltration water is diverted from the Llobregat river and enters the first pond for settling of the fine sediment; water then enters the infiltration pond, constructed over coarse geologic materials.

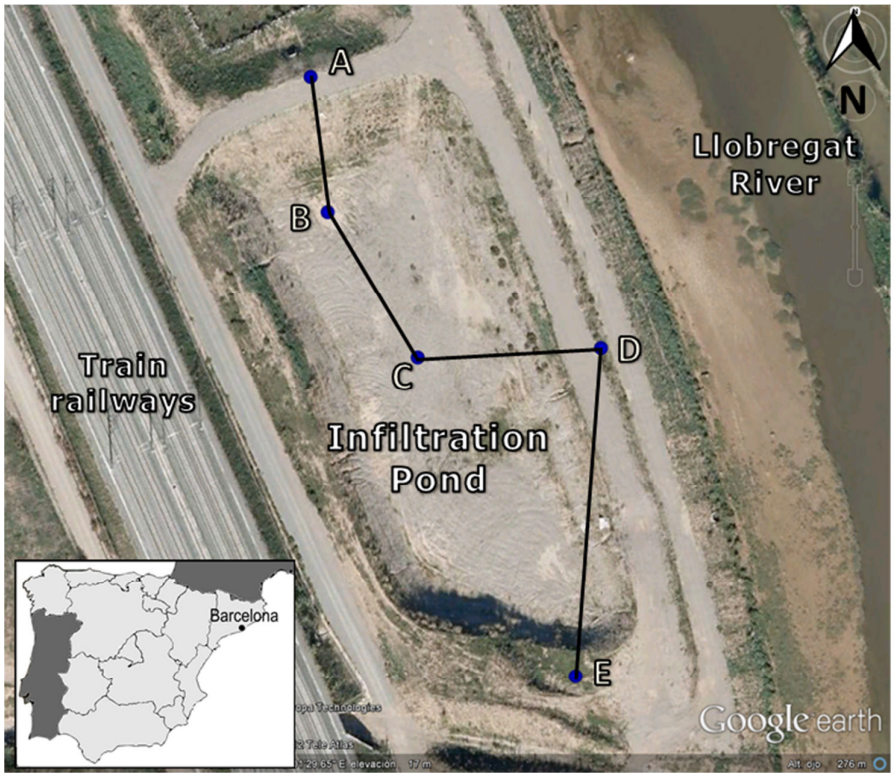

Figure 4-1. Infiltration Pond close to Barcelona, Spain. Labeled blue dots indicate the location of piezometers, the black line indicates the location of the composite cross section shown in Figure 4-2.

The site is located over quaternary fluvial deposits associated to the Llobregat river (Institut Geològic de Catalunya, 2011). Geological loggings of recovered cores from piezometers built close to and into the infiltration pond were used to construct a composite geological cross-section for the site (Figure 4-2). This cross-section was enriched with information provided by a natural gamma-ray geophysical log campaign, made on selected piezometers at the site.

According to the information gathered at the site, the upper layer is composed of fine sediments (silty-sand, sandy-silt) with organic matter, and it is approximately 2-5 meters thick (designated here as top soil). This layer is underlain by a 17-20 m thick very permeable layer of coarse sediments (gravel and sandy-gravel), displaying lenses of clay with a maximum thickness of 1-2.5 meters. At the bottom, there is a low permeability layer of blue-clay associated to a regional Pliocene marls unit (Gàmez et al., 2007).

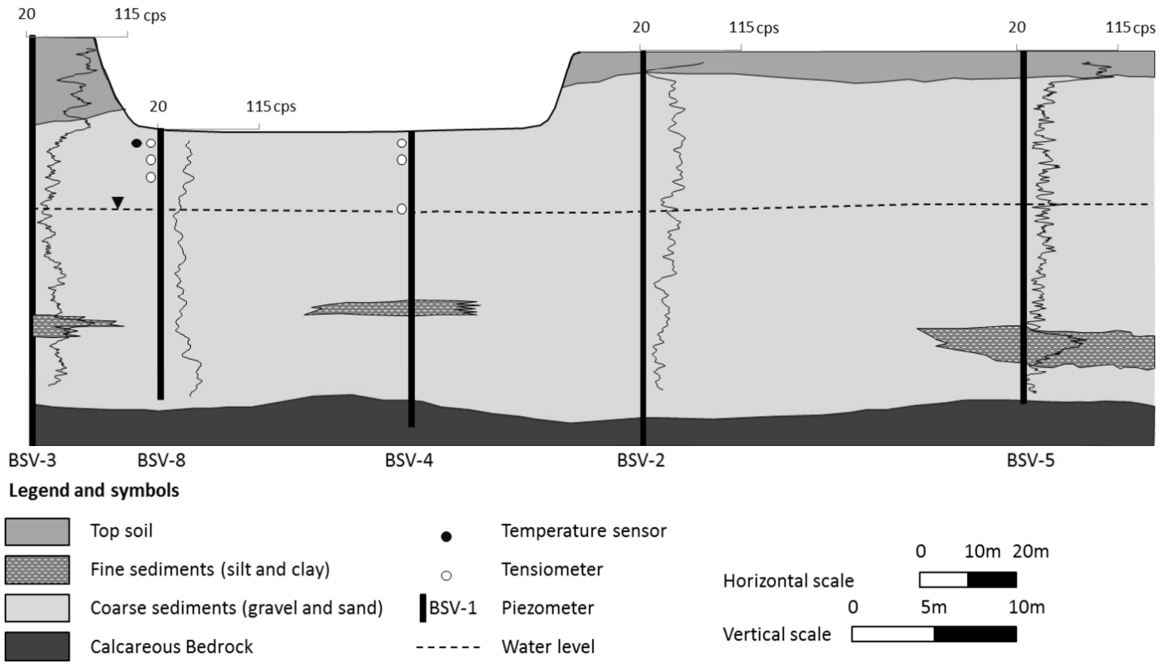

Figure 4-2. Composite simplified geological cross-section through the experimental infiltration pond based on the projections of the core logging interpretation from piezometers A, B, C and E, and natural gamma-ray geophysical campaign from piezometers A, B, D and E. See Figure 4-1 for surface location of the cross-section. Layers with low natural gamma-ray values

are interpreted as coarse grain size units (sand or gravel), and layers with high natural gamma-ray values are interpreted as fine grain size units (silt or clay).

Grain sieve analysis from samples taken at different depths and locations within the pond, confirm that a highly permeable material exists at the site. The hydraulic conductivity value obtained after the Kozeny-Carman formulation yields a range value of 10^{-4} to 10^{-2} m/s (see

Table 4-1), indicative of well-sorted gravels.

Table 4-1. Hydraulic conductivity values from grain sieve analysis in five sampling points within the pond, with the corresponding depths were samples were taken.

Approximate Depth (cm)	**Hydraulic Conductivity (m/s)**
20-65	$1x10^{-3}$
75-85	$9x10^{-4}$
106-126	$1x10^{-2}$
0-24	$1x10^{-4}$
38-43	$3x10^{-4}$

4.2.2. EXPERIMENTAL DESIGN

Experimental infiltration campaigns where performed in the spring of 2009 and winter of 2011 at an Artificial Recharge facility. Each infiltration campaign lasted more than 90 days; for this research, however, we have considered only the time frame during which the level on the infiltration pond was higher than 30 cm at the measuring point, at that altitude the water covered the entire pond floor, that is, 27 days for the first campaign and 18 days for the second.

Surface water level (SWL) and temperature at the infiltration pond were measured during both periods, with surface water temperatures ranging between 2ºC and 25ºC. These two parameters fluctuated daily, they however, display a phase shift, as shown in Figure 4-3 and Figure 4-4.

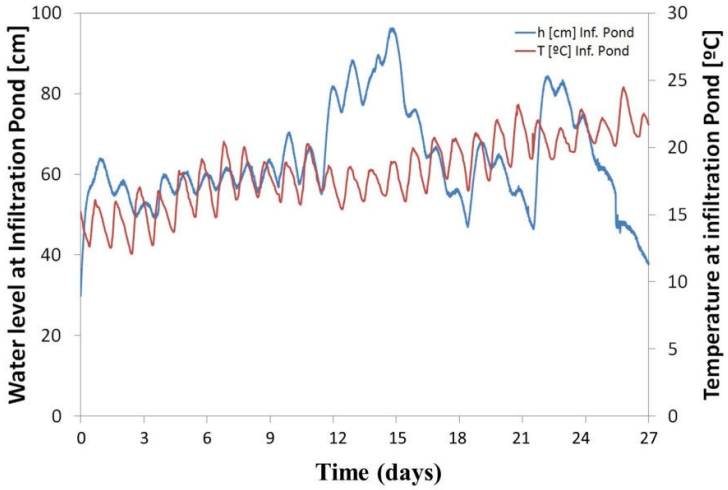

Figure 4-3. Water level (h) and temperature (T) on the pond, during the spring infiltration campaign.

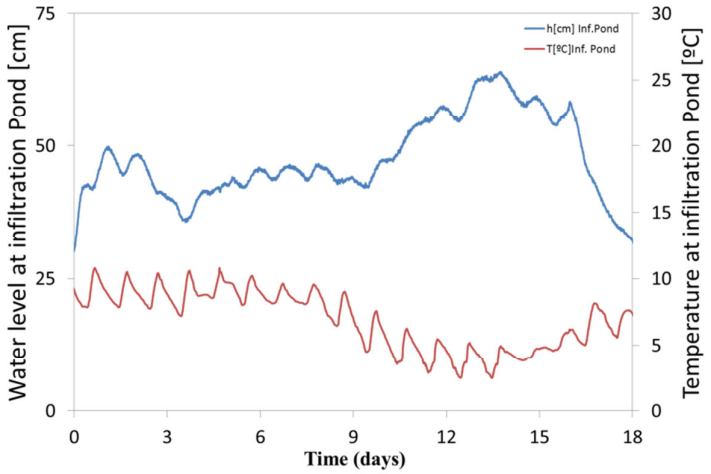

Figure 4-4. Water level (h) and temperature (T) on the pond, during the winter infiltration campaign.

Major changes in the incoming flow [Q_{in}] to the pond, are correlated with observed large head variations in the surface water level (see Figure 4-5 and Figure 4-6), however, a daily fluctuating pattern is not observed in Q_{in}, discarding it as the cause of the daily SWL fluctuations observed on the pond.

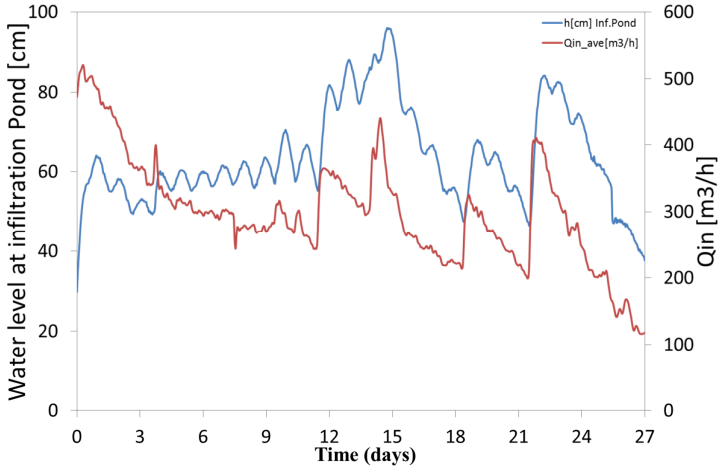

Figure 4-5. Incoming flow (Qin) through time measured at the inlet. Major changes (increases and decreases) have a direct influence on water level at the

infiltration pond; water level daily fluctuations at the pond, however, do not seem to be related with the Qin. [spring recharge]

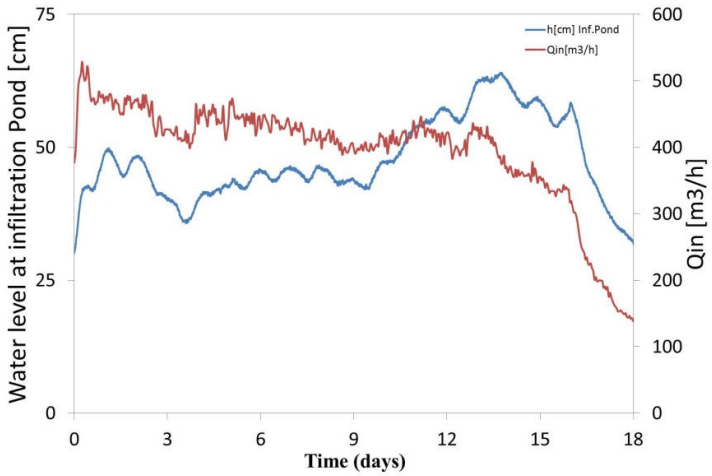

Figure 4-6. Incoming flow (Q_{in}) measured at the inlet as a function of time, compared to water level daily fluctuations at the pond. No direct correlations is visible [winter recharge]

In order to calculate the infiltrating flow (Q_{out}), we consider the mass balance equation:

$$Q_{in}\rho_w C_w T - Q_{out}\rho_w C_w T = \frac{d}{dt}(V_w \rho_w C_w T) \qquad \text{Equation 4.2}$$

Where ρ_w , C_w, T, V_w are water density, specific heat, temperature, and volume in the pond, respectively. All four parameters are variable with time *t*.

Rearranging Equation 4.2 and discretizing the derivative in time, it is possible to find an explicit expression for Q_{out} at time t+1 by assuming that variations in ρ_w , C_w, V_w, change slowly in time. Defining A as wet surface area (also variable in time)

$$Q_{out}^{t+1} = Q_{in}^{t+1} - \frac{A^{t+1}h^{t+1} - A^t h^t}{\Delta t} \quad \text{Equation 4.3}$$

The values obtained for Q_{out} from (Equation 4.3) are shown in Figure 4-7 and Figure 4-8 for the two periods of time studied. Daily variations on infiltration rates, also out of phase with respect to the water level at the pond, are visible in such figures.

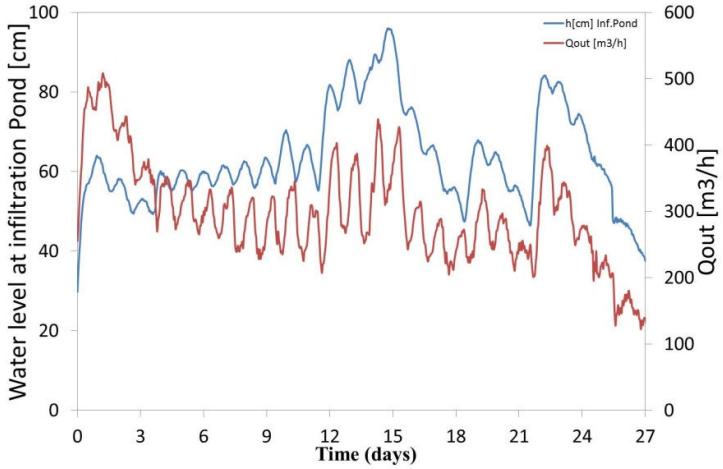

Figure 4-7. Calculated infiltrating flow (Q_{out}) from the mass balance Equation 4.3 and water level (h) measured at the pond. Notice that Q_{out} is out of phase with respect to h [spring recharge period].

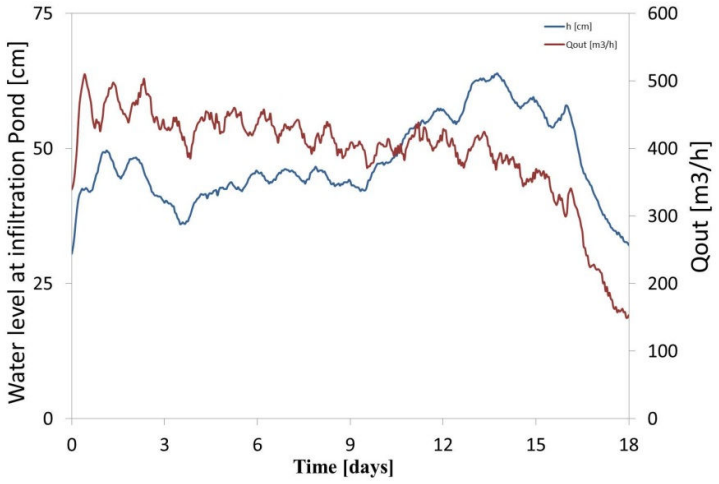

Figure 4-8. Calculated infiltrating flow (Q_{out}) from the mass balance Equation 4.3 and water level (h) measured at the pond. Notice that Q_{out} is out of phase with respect to h [winter recharge period].

Considering Q_{out} and the area of the pond we calculated an infiltration rate following a simple approach where $I= Q_{out}/A$ and show that the infiltration rate varies through time and that it is also out of phase with respect to SWL.

An energy balance considering the calculated Q_{out}, renders a very good correlation between the measured temperature at the infiltration pond and that calculated with the energy balance.

Groundwater levels and temperatures were measured during the infiltration campaigns, along with tensiometer readings (during both periods) and vadose zone temperature (during the second period) installed at different depths below the pond.

The aquifer beneath the pond is an unconfined granular aquifer. Groundwater level beneath the bottom of the pond is approximately 6 meters deep. During the flooding experiments groundwater fluctuated daily, with variations of up to 50 cm during the spring experiment and 35 cm during the winter.

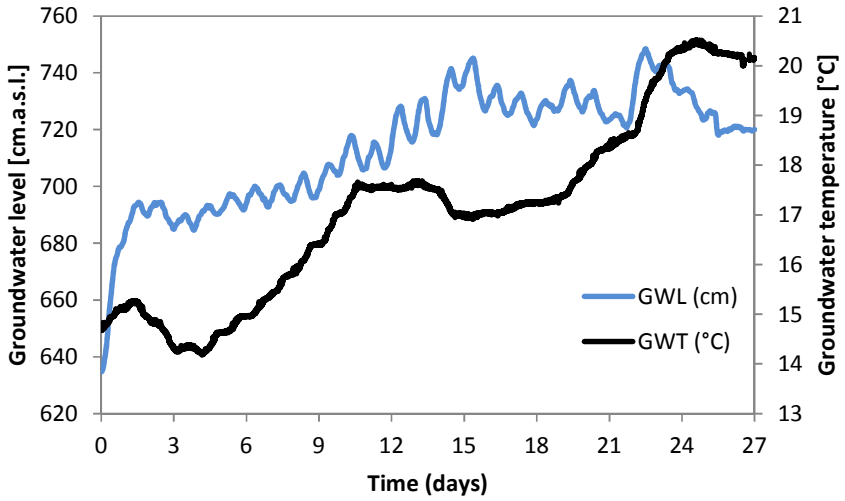

Figure 4-9. Groundwater levels (GWL) and temperatures (GWT) below the infiltration pond, during the first experiment.

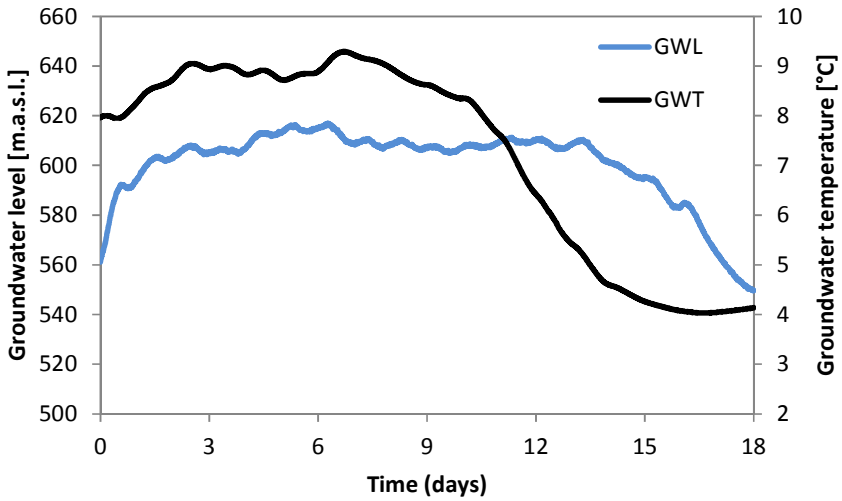

Figure 4-10. Groundwater levels (GWL) and temperatures (GWT) below the infiltration pond, during the second experiment.

Tensiometers were installed at three different depths in the vadose zone (1.0 m, 1.9 m and 4.9 m below the surface of the pond) and provided information relative to the soil water potential as shown in figures 11 and 12. In these two figures it can be observed daily fluctuation in the readings, indicating decametric daily variations in the hydraulic head.

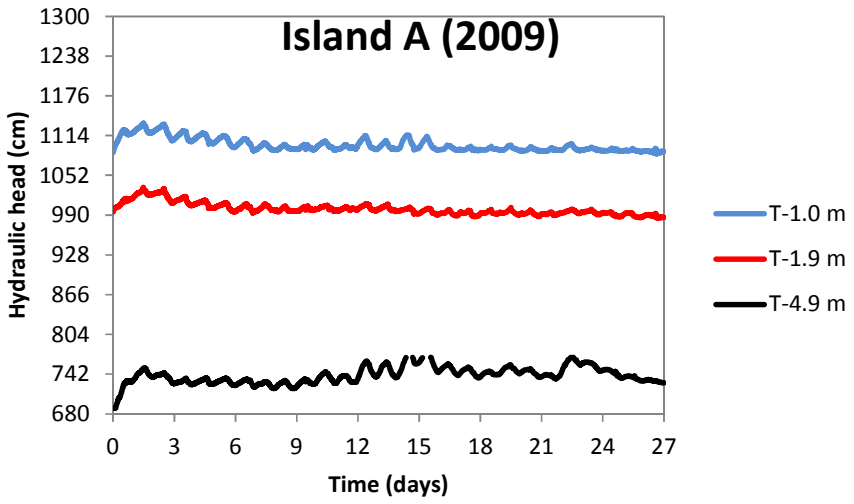

Figure 4-11. Measured pressure head in the tensiometers located at 1.0 m, 1.9 m and 4.9 m deep below the infiltration pond, for the spring flooding event.

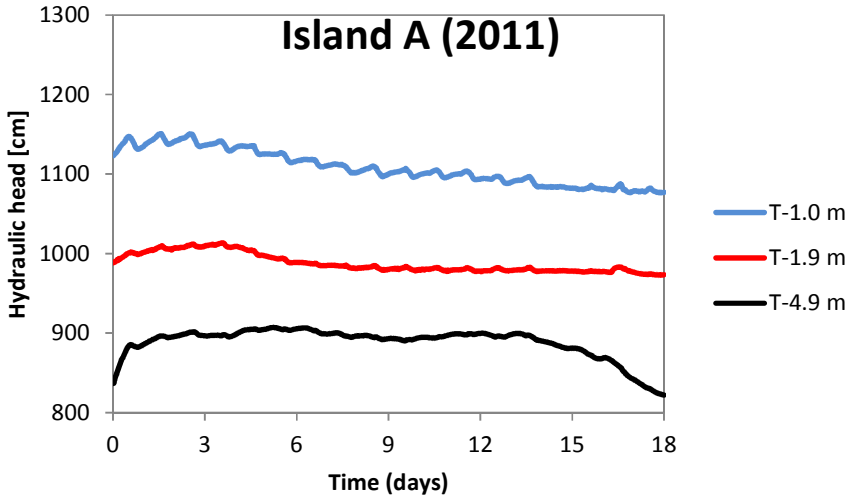

Figure 4-12. Measured pressure head in the tensiometers located at 1.0 m, 1.9 m and 4.9 m deep below the infiltration pond, for the winter flooding event.

For the winter flooding event, information relative to the temperature was recorded at one meter depth. Even at a depth of 1m, daily variations in temperature are clearly observed, with ranges that are above 1ºC in some cases.

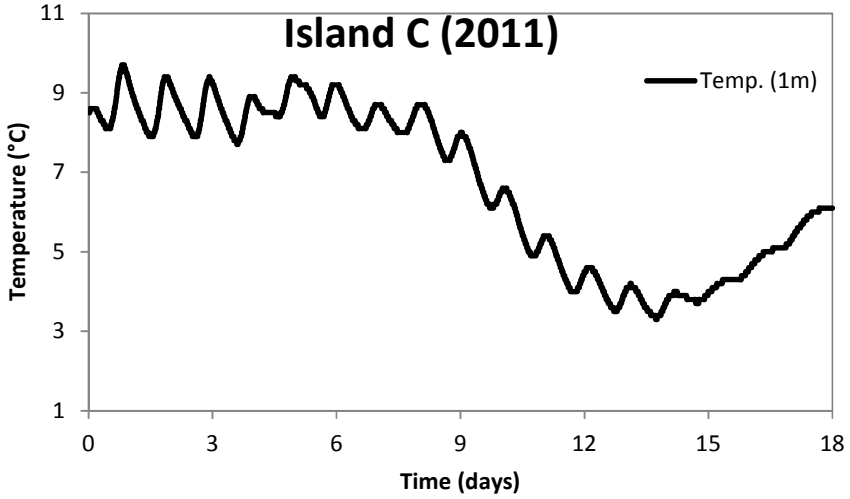

Figure 4-13. Temperature measurements taken at one meter below the infiltration pond, during the winter infiltration event. Even at a 1m depth, daily variations in temperature are clearly visible.

4.2.3. NUMERICAL MODELING: DESCRIPTION AND PARAMETER DETERMINATION

The Hydrus-1D code (Simunek et al., 2013) was used to simulate 1D vertical water and heat flow for infiltration field conditions. This code solves Richards equation for variably saturated water flow:

$$\frac{\partial \theta}{\partial t} = \frac{\partial}{\partial z}\left[K(h)\frac{\partial h}{\partial z} - K(h)\right] - S(t,z,h) \qquad \text{(Equation 4.4)}$$

where θ is the volumetric water content ($cm^3 \cdot cm^{-3}$) at soil-water pressure head h (cm); t is time (day); z the vertical space coordinate (cm) positive downward; K is hydraulic conductivity ($cm \cdot day^{-1}$); and S is the sink term.

The soil hydraulic properties were described with the van Genuchten-Mualem constitutive relationships

$$\theta(h) = \begin{cases} \theta_r + \dfrac{\theta_s - \theta_r}{(1 + |\alpha h|^n)^m} & h \leq 0 \\ \theta_s & h > 0 \end{cases} \qquad \text{(Equation 4.5)}$$

where θ_r and θ_s are the residual and saturated water contents, respectively ($cm^3 \cdot cm^{-3}$); α $(> 0, in\ cm^{-1})$ is related to the inverse of the air-entry pressure; n (> 1) is a measure of the pore-size distribution; and $m = 1 - 1/n$ (van Genuchten, 1980).

The corresponding Van Genuchten-Mualem hydraulic conductivity function, K(h), is

$$K(h) = \begin{cases} K_s S_e^l \left[1 - \left(1 - S_e^{1/m}\right)^m\right]^2 & h \leq 0 \\ K_s & h > 0 \end{cases} \qquad \text{(Equation 4.6)}$$

where

$$S = \frac{\theta - \theta_r}{\theta_s - \theta_r}, \qquad m - 1 - (1/n)$$

where K_s is the saturated hydraulic conductivity ($cm \cdot day^{-1}$) and l is an empirical pore-connectivity parameter.

The hydraulic parameters θ_r, θ_s, n, α and l were taken from the database available in Schaap et al. (2001). These authors use a pedotransfer function software that uses a neural network model to predict hydraulic parameters from soil texture and related data. We used the values indicated by the authors for sand, compiled in Table 4.2. For K_S, however, we used the value calculated for a sand horizon below the infiltration pond, corresponding to the finest sediment sample observed in the cross sections (see Figure 4-2).

Table 4-2. Hydraulic parameters values used in the model of the infiltration process, taken from Schaap et al. (2001) database, with the parameters corresponding to a sand. The value for K_S corresponds to a fine sand.

θ_r [-]	θ_s [-]	α [1/cm]	n [-]	K_S [cm/day]	l [-]
0.053	0.375	0.0352371	3.17687	225	-0.93

We performed a one-dimensional (1-D) heat transport modeling considering the case of an infiltration pond. Considering the cross-section shown in Figure 4-2, we have assumed a highly permeable material under the infiltration pond, and therefore, consider a 6 m thick, unsaturated, single layer for the 1-D model.

The thermal conductivity can be parameterized as a function of soil texture and soil water-content. There are different functions of thermal conductivity, one function is presented by Chung & Horton (1987):

$$\lambda(\theta) = b_1 + b_2\theta + b_3\theta^{0.5} \quad \text{(Equation 4.7)}$$

where b_1, b_2, and b_3, are empirical parameters ($W \cdot m^{-1} \cdot K^{-1}$). For the simulations we considered the default values presented in HYDRUS-1D for sand, and are respectively equal to 0.228, -2.406, and 4.909.

4.2.4. Numerical Modelling: Initial and Boundary Conditions

A Dirichlet-type boundary condition was imposed on the top and the bottom of the model, both for head and temperature. The values correspond with the measurements taken on the field. The values assigned at the top boundary (surface of the pond) were obtained from the surface water level and temperature measured on the infiltration pond and thus are time variable. The groundwater level and temperature assigned at the bottom boundary were also assigned from existing measurements registered on a piezometer installed within the pond.

For the initial conditions, both the hydraulic head and the initial temperature for the vadose zone were considered to diminish linearly with depth within a range of values limited by the top and bottom boundary values.

4.3. Results and discussion

The results of the water temperature and hydraulic conductivity variations reported in this section include hydraulic conductivity profiles at different times and the evolution

of hydraulic heads with the simulation time (27 and 18 days for experiment one and two, respectively). The spatial discretization involved nodes separated 10 cm, leading to a total number of nodes of 94. The time steps were automatic selected by the code. The initial time step was 0.0034 days, with a minimum time step of 6.94×10^{-4} days (one minute), and a maximum time step set to 2.08×10^{-2} days (30 minutes).

Figure 4-14 shows the water temperatures measured at 1 m beneath the infiltration pond compared to those given by the numerical model. The agreement can be considered quite good, especially for the first 15 days; the model appears to deteriorate for the last three days; it however captures the increasing trend measured on the field.

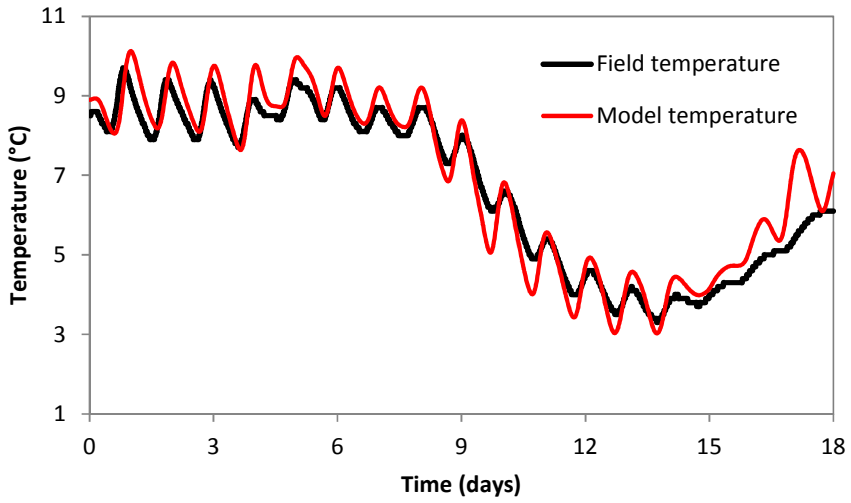

Figure 4-14. Water temperature measured and model at one meter beneath the infiltration pond. Only the winter infiltration period is presented.

Figures 15 and 16 show the hydraulic head simulation results for points located at 1.0 m, 1.9 m and 4.9 m below the infiltration pond surface. The results show important fluctuations in the head values.

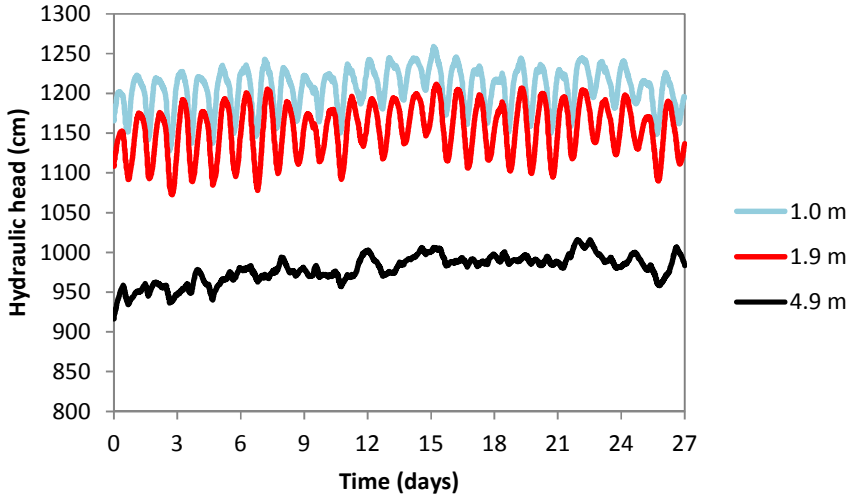

Figure 4-15. Model hydraulic head for the first infiltration event at different depths.

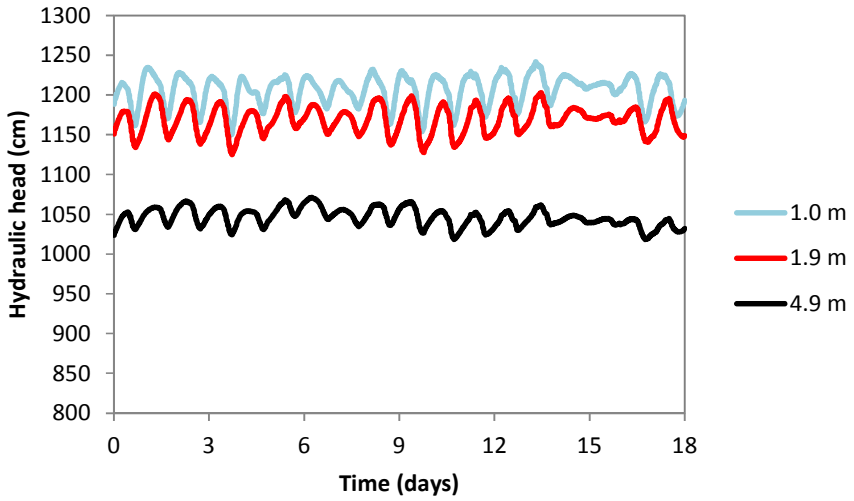

Figure 4-16. Model hydraulic heads for the winter infiltration event.

Figures 17 and 18 present modeled hydraulic conductivity values in the soil profile for selected times, presenting high, low and intermediate K values. In the first infiltration experiment, K varied between 185.0 cm/day and 248.1 cm/day, resulting in a 34% difference. In Figure 4-17 it can also be observed the daily fluctuations in the soil profile and rapid changes in the position in K value horizons as indicated by times 15.5 and 16.0 days.

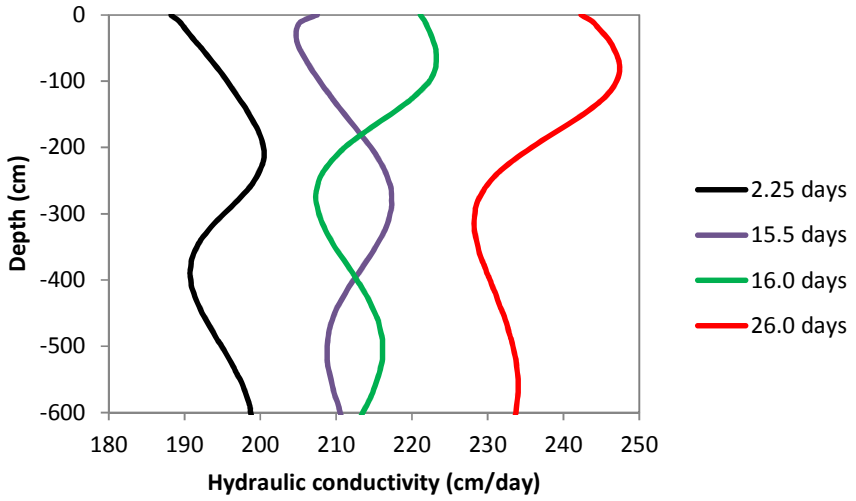

Figure 4-17. Hydraulic conductivity variation on the soil profile beneath the infiltration pond for selected times, corresponding to the first infiltration event. Times 2.25 and 26.0 days represent respectively lower and higher water temperature entering the soil. Times 15.5 and 16.0 days are shown for comparison as intermediate hydraulic conductivity values and to see the effect of variations within a given day.

Figure 4-18 presents K profiles for the second infiltration event, showing extreme cases within the 18 days period, during that particular event. K values ranged between 138.7 cm/day and 176.6 cm/day, showing a 27% difference in hydraulic conductivity during that time.

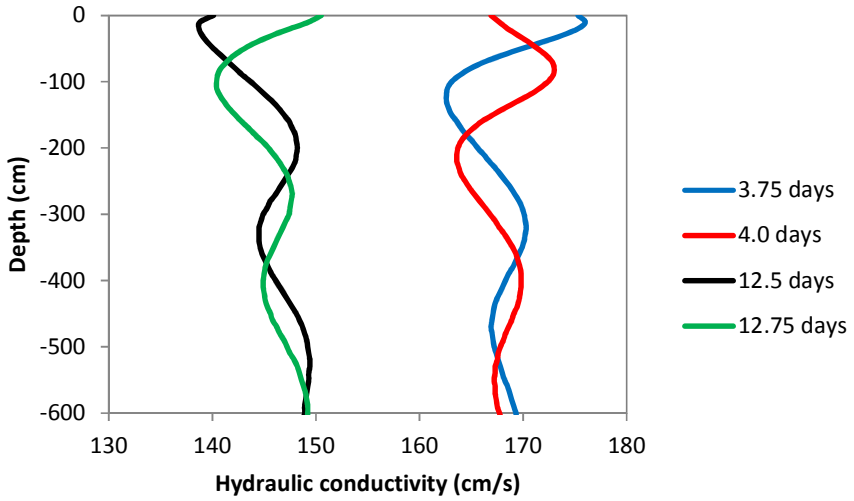

Figure 4-18. Hydraulic conductivity variation on the soil profile beneath the infiltration pond for selected times, according to the model for the second event.

Our model shows how the variation in water temperature at the pond affects the water temperature in the vadose zone. Due to its high permeability, water travels at a high rate within the sediment under the pond; therefore, water with different temperature is present at different depths within the vadose zone at any time during the recharge period. This situation translates into different K values within the same layer, even though all the other parameters are the same for this layer (i.e. the same grain size).

Considering both events, the hydraulic conductivity values ranged between 138.7 cm/day and 248.1 cm/day, meaning a 79 % variation. In figures 17 and 18 it can also be observed variations within the same day, caused by the daily water temperature fluctuation, which causes different K values in depth, just by the difference in water temperature alone.

This variations of K with time in the sediment below the infiltration pond when water with varying temperature enters the sediment, causes the infiltration velocity change with time and produces the observed fluctuation on the infiltration pond. Our model indicates that the water retention curve, and correspondingly, the variations of hydraulic conductivity with depth, is key in the management of infiltration recharge. As shown, water temperature fluctuations might even double infiltration recharge on a typical range for temperate climates. These observations should be considered when designing for infiltration management practices.

5. CONCLUSIONS

The following conclusions presented here, summarizes the conclusions presented in chapters 2, 3 and 4.

- The degree of correlation between conductivity values associated with interpretation methods based on impeller flowmeter measurements and particle-size distributions has then been explored. The IFM method provides estimates within a given borehole that somehow smooth or dampen actual (small-scale) natural variability, because the pressure distribution around the measuring device can be far from the theoretical distribution envisioned for homogeneous systems. On the other hand, GSD-based conductivities are only influenced by the local composition of the tested granular material. The latter can display significant spatial contrasts, resulting in larger sills and shorter ranges than those associated with IFM interpretations. These findings are consistent with the fact that the two types of estimates analyzed can be associated with different, albeit of similar order of magnitude, support (measurement) scales. Precise characterization of the support scale of any given information is thus needed to properly include hydraulic conductivity data into numerical models. This is particularly needed for the assessment of the support scale linked IFM conductivity measurement, which is still not completely clear.

- A non-parametric method, SKR, designed for image processing (Takeda et al. 2007), has been tested for a different field, facies delineation. This method performance was compared with the nearest neighbor classification, a method that has proven to be more efficient than others when used for facies delineation

by Tartakovsky et al. (2007). Four synthetic scenarios (Figure 3-1) were used for performance comparison between these two methods, the first two are identical to the figures presented by Tartakovsky et al. (2007), and the other two figures are new, one inspired on a meander (from the Ebro river, Spain) and the other, a simple geometric figure, a circle. Our results indicate that the SKR outperformed the NNC in most cases. Two criteria were considered for the SKR: SKR(0) and SKR(%); these distinctions were defined following the criteria indicated on (Equation 3.30). The fact that SKR(%) outperforms the NNC is a breakthrough for facies delineation, especially when we consider that the difference in error fractional error is more evident when a low sampling density is considered. This finding leads to believe that SKR(%) can be employed as an useful tool on real cases, when scattered and few sampling data are available.

- A one-dimensional (1-D) heat transport modeling considering the case of an infiltration pond was presented. The effect of water temperature fluctuation on the hydraulic conductivity profile of coarse sediments beneath an artificial recharge facility is modeled and compared with field data. Due to the high permeability, water travels at a high rate, and therefore also water with different temperature is also present on the sediment under the pond at different moments; this translates into different hydraulic conductivity values within the same layer, even though all the other parameters remain constant within the layer. Differences of almost 79% in hydraulic conductivity were observed for the model temperatures (2 °C – 25 °C). These variations of hydraulic conductivity in the sediment below the infiltration pond when water with varying temperature

enters the sediment, causes the infiltration velocity change with time and produces the observed fluctuation on the field measurements.

6. REFERENCES

American Association for Laboratory Accreditation . (2005). *P103d – Annex: Policy on Estimating Measurement Uncertainty for Construction Materials & Geotechnical Testing Labs.* .

Barr, D. W. (2005). Discussion of "Goodbye Hazen; hello, Kozeny-Carman" by W. David Carrier III. *Journal of Geotechnical and Geoenvironmental Engineering, 131*(8), 1057-1058.

Beckie, R. (1996). Measurement scale, network sampling scale, and groundwater model parameters. *Water Resources Research, 32*(1), 65–76.

Bennett, K. P., & Campbell, C. (2000). Support vector machines: Hype or hallelujah? *SIGKDD Explorations, 2*(2).

Beyer, W. (1964). Zur Bestimmung der Wasserdurchlässigkeit von Kiesen und Sanden aus der Kornverteilungskurve [On the determination of the hydraulic conductivity of gravel and sand based on grain size distribution]. *Wasserwirtschaft. Wassertech, 14*(6), 165–169.

Boman, G. K., Molz, F. J., & Boone, K. D. (1997). Borehole flowmeter application in fluvial sediments: Methodology, results, and assessment. *Ground Water, 35*(3), 443-450.

Braga, A., Horst, M., & Traver, R. G. (2007). Temperature Effects on the Infiltration Rate through an Infiltration Basin BMP. *Journal of Irrigation and Drainage Engineering, 133*(6), 593-601.

References

Bughin, E., Blanc-Feraud, L., & Zerubia, J. (2008). Satellite image reconstruction from an irregular sampling. *Proceedings IEEE International Conference on Acoustics, Speech and Signal Processing (ICASSP), 2*(3), 849-852. doi: 10.1109/ICASSP.2008.4517743.

Butler, J. J. (2005). Hydrological methods for estimation of spatial variations in hydraulic conductivity. In Y. Rubin, & S. S. Hubbard (Eds.), *Hydrogeophysics* (pp. 23-58). Netherlands: Springer.

Cardenas, M. B., & Zlotnik, V. A. (2003). Constant-head injection tests: a simple method for streambed permeability estimation. *Ground Water, 41*(6), 867-871.

Carrier, W. D. (2003). Goodbye, Hazen; Hello, Kozeny-Carman. *Journal of Geotechnical and Geoenvironmental Engineering, 129*(11), 1054-1056.

Cheng, C., & Chen, X. (2007). Evaluation of methods for determination of hydraulic properties in an aquifer–aquitard system hydrologically connected to a river. *Hydrogeology Journal , 15*, 669-678.

Chung, S.-O., & Horton, R. (1987). Soil Heat and Water Flow with a Partial Surface Mulch. *Water Resources Research, 23*(12), 2175-2186.

Constantz, J. (1998). Interaction between stream temperatures, streamflow, and groundwater exchanges in alpine streams. *Water Resources Research, 34*(7), 1609-1615.

Constantz, J., & Murphy, F. (1991). The Temperature Dependence of Ponded Infiltration under Isothermal Conditions. *Journal of Hydrology, 122*, 119-128.

References

Constantz, J., Thomas, C. L., & Zellweger, G. (1994). Influence of diurnal variations in stream temperature on streamflow loss and groundwater recharge. *Water Resources Research, 30*(12), 3253-3264.

Custodio, E., & Llamas, R. M. (1984). *Hidrología Subterránea [Hydrogeology]*. Barcelona, Spain.

Daoudi, M., Ghorbel, F., Mokadem, A., Avaro, O., & Sanson, H. (1999). Shape distances for contour tracking and motion estimation. *Pattern Recognition*, 1297-1306.

Dixon, P. M. (2002). Nearest neighbour methods. In A. H. El-Shaarawi, & W. W. Piegorsch (Eds.), *Encyclopedia of Environmetrics, vol. 3* (pp. 1370– 1383). New York: John Wiley.

Fetter, C. W. (2001). *Applied Hydrogeology* (Fourth ed.). Englewood Cliffs, New Jersey: Prentice Hall.

Fogg, G. E., Noyes, C. D., & Carle, S. F. (1988). Geologically based model of heterogeneous hydraulic conductivity in an alluvial setting. *Hydrogeology Journal, 6*, 131-143.

Franke, R. (1982). Scattered Data Interpolation: Tests of Some Methods. *Mathematics of Computation, 38*(157), 181-200.

Gallardo, A. H., & Marui, A. (2007). Hydraulic characteristics of sedimentary deposits at the J-PARC proton-accelerator, Japan. *Earth Sciences Research Journal, 11*(2), 139-154.

References

Gàmez, D., Vàzquez-Suñé, E., Simó, T., Carrera, J., Ibañez, X., & Niñerola, J. M. (2007). Nueva interpretación del modelo geológico conceptual de los acuíferos pleistocenos del delta de Llobregat (Barcelona, España) (comunicación libre). In *Jornadas Internacionales "De la toma de datos y la realización de modelos de agua subterránea a la gestión integrada", 4-8 Octubre 2005* (pp. 323-328). Alicante: IGME.

Guadagnini, L., Guadagnini, A., & Tartakovsky, D. M. (2004). Probabilistic reconstruction of geologic facies. *Journal of Hydrology, 294*, 57-67.

Hess, K. M., Wolf, S. H., & Celia, M. A. (1992). Large-scale natural gradient tracer test in sand and gravel, Cape Cod, Massachusetts – 3. Hydraulic conductivity variability and calculated macrodispersivities. *Water Resources Research, 28*(8), 2011-2027.

Hufschmied, P. (1986). Estimation of three-dimensional statistically anisotropic hydraulic conductivity field by means of a single well pumping test combined with flowmeter measurements. *Hydrogeologie, 2*(163-174).

Institut Geològic de Catalunya. (2011). *Mapa geològic de les zones urbanes 1:5 000, Sant Feliu de Llobregat 286-126(420-6-6)* (First ed.). Barcelona: Institut Cartogràfic de Catalunya.

International Organization of Standardization-GUM. (1995). *Guide to the expression of uncertainty in measurements.* Geneva, Switzerland.

Isaaks, E. H., & Srivastava, R. M. (1990). *An Introduction to Applied Geostatistics.* New York: Oxford University Press.

References

Journel, A. G. (1983). Non-parametric estimation of spatial distribution. *Mathematical Geology, 15*(3).

Kasenow, M. (2002). *Determination of hydraulic conductivity from grain size analysis.* Ranch, CO: Water Resources Publications.

Lin, C., Greenwald, D., & Banin, A. (2003). Temperature dependece of infiltration rate during large scale water recharge into soils. *Soil Science Society of America Journal, 67*, 487-493.

Lin, S. C., & Chen, C. T. (2008). Reconstructing vehicle license plate Image from low resolution images using nonuniform interpolation method. *International Journal of Image Processing, 1*(2).

Martac, E., & Ptak, T. (2003). *Data sets for transport model calibration/validation, parameter upscaling studies and testing of stochastic transport models/theory.* Report D16 of Project "Stochastic Analysis of Well-Head Protection and Risk Assessment—W-SAHaRA", EU contract EVK1-CT-1999-00041, Milan, Italy (2003).

McKenzie, N. J., & Cresswell, H. P. (2002). Selecting a method for hydraulic conductivity. In N. McKenzie, K. Coughlan, & H. Cresswell, *Soil physical measurement and interpretation for land evaluation* (Vol. 5, pp. 90-107). Melbourne, Australia: CSIRO Publishing.

Molz, F. J., Bowman, G. K., Young, S. C., & Waldrop, W. R. (1994). Borehole flowmeters – field application and data analysis. *Journal of Hydrology, 163*(3-4), 347–371.

References

Molz, F. J., Morin, R. H., Hess, A. E., Melville, J. G., & Güven, O. (1989). The impeller meter for measuring aquifer permeability variations: evaluation and comparison with other tests. *Water Resources Research, 25*(7), 1677–1683.

Muskat, M. (1937). *The Flow of Homogeneous Fluids Through Porous Media* (First ed.). New York: McGraw-Hill.

Neuman, S. P., & Di Federico, V. (2003). Multifaceted nature of hydrologic scaling and its interpretation. *Reviews of Geophysics*(3), 1014, doi:10.1029/2003RG000130.

Neuman, S. P., Blattstein, A., Riva, M., Tartakovsky, D. M., Guadagnini, A., & Ptak , T. (2007). Type curve interpretation of late-time pumping test data in randomly heterogeneous aquifers. *Water Resources Research, 43*(10), W10421.

Neuman, S. P., Riva, M., & Guadagnini, A. (2008). On the geostatistical characterization of hierarchical media. . *Water Resources Research, 44*(2), W02403 .

Odong, J. (2007). Evaluation of Empirical Formulae for Determination of Hydraulic Conductivity based on Grain-Size Analysis. *Journal of American Science, 3*(3), 54-60.

Payne, F. C., Quinnan, J. A., & Potter, S. T. (2008). *Remediation Hydraulics.* Boca Raton, Florida.

Rehfeldt, K. R., Hufschmied, P., Gelhar, L. W., & Schaefer, M. E. (1989). *The borehole flowmeter technique for measuring hydraulic conductivity variability. Report No. EN 6511.* Electric Power Research Institute, Palo Alto, CA.

Riera, J., Vazquez-Suñe, E., Sanchez-Vila, X., & Dentz, M. (2010). On the selection of the best alternative for deriving hydraulic conductivity from grain sieve analysis. *Ground Water, submitted*, Submitted.

Ritzi, R. W., Jayne, D. F., Zahradnik, A. J., Field, A. A., & Fogg, G. E. (1994). Geostatistical Modeling of Heterogeneity in Glaciofluvial, Buried-Valley Aquifers. *Ground Water, 32*(4), 666-674.

Riva, M., Guadagnini, A., Fernandez-Garcia, D., Sanchez-Vila, X., & Ptak, T. (2008). Relative importance of geostatistical and transport models in describing heavily tailed breakthrough curves at the Lauswiesen site. *Journal of Contaminant Hydrology, 101*, 1-13.

Riva, M., Guadagnini, L., & Guadagnini, A. (2010). Effects of uncertainty of lithofacies, conductivity and porosity distributions on stochastic interpretations of a field scale tracer test. *Stochastic Environmental Research Risk Assessment*(24), 955-970.

Riva, M., Guadagnini, L., Guadagnini, A., Ptak, T., & Martac, E. (2006). Probabilistic study of well capture zones distributions at the Lauswiesen field site. *Journal of Contaminant Hydrology, 88*, 92-118.

Ronan, A. D., Prudic, D. E., Thodal, C. E., & Constantz, J. (1998). Field study and simulation of diurnal temperature effects on infiltration and variably saturated flow beneath an ephemeral stream. *Water Resources Research, 34*(9), 2137-2153.

Rorabaugh, M. I. (1963). Streambed Percolation in Development of Water Supplies. In R. Bentall (Ed.), *Methods of Collecting and Interpreting Groundwater Data* (Vols. 1544-H, pp. 47-62). U.S. Geological Survey Water Supply Paper.

Sack-Kühner, B. T. (1996). Einrichtung des Naturmeßfeldes "Lauswiesen Tübingen", Erkundung der hydraulischen Eigenschaften, Charakterisierung der Untergrundheterogenität und Vergleich der Ergebnisse unterschiedlicher Erkundungsverfahren. *[Installation of the natural measuring field "Lauswiesen Tübingen", investigation of the hydraulic characteristics, characterization of the underground heterogeneity and comparison of the results for different investigation procedures]*. M.Sc. Thesis, University of Tübingen, Geological Institute.

Sanchez-Vila, X., Guadagnini, A., & Carrera, J. (2006). Representative hydraulic conductivities in saturated groundwater flow. *Reviews of Geophysics, 44*(3), RG3002.

Schaap, M. G., Leij, F. J., & van Genuchten, M. T. (2001). ROSETTA: a computer program for estimating soil hydraulic parameters with hierarchical pedotransfer functions. *Journal of Hydrology, 251*(3-4), 163-176.

Simunek, J., Sejna, M., Saito, H., Sakai, M., & van Genuchten, M. T. (2013). *The HYDRUS-1D Software Package for Simulating the One-Dimensional Movement of Water, Heat, and Multiple Solutes in Variably-Saturated Media version 4.16.* University of California-Riverside Research Reports.

Stauffer, T. B., & Manoranjan, V. S. (1994). The use of grain-size analysis field-data to study hydraulic conductivity variability. *Aviation, Space, and Environmental Medicine, 65*(5), A125-A130.

Strebelle, S. (2000). *Sequential simulation drawing structures from training images.* Unpublished doctoral dissertation, Stanford University.

Takeda, H., Farsiu, S., & Milanfar, P. (2007, February). Kernel Regression for Image Processing and Reconstruction. *IEEE Transactions on Image Processing, 16*(2).

Tarbuck, E. J., & Lutgens, F. K. (2002). *Earth: An Introduction to Physical Geology* (Seventh ed.). Prentice Hall.

Tartakovsky, D. M., & Wohlberg, B. E. (2004). Delineation of geologic facies with statistical learning theory. *Geophysical Research Letters, 31*, L18502, doi:10.1029/2004GL020864.

Tartakovsky, D. M., Wohlberg, B., & Guadagnini, A. (2007). Nearest-neighbor classification for facies delineation. *Water Resources Research, Vol. 43*, W07201, doi: 10.1029/2007WR005968.

Tidwell, V. C., & Wilson, J. L. (1999a). Permeability upscaling measured on a block of Berea Sandstone: Results and interpretation. *Mathematical Geology, 31*(7), 749-769.

Tidwell, V. C., & Wilson, J. L. (1999b). Upscaling experiments conducted on a block of volcanic tuff: Results for a bimodal permeability distribution. *Water Resources Research, 35*(11), 3375-3387.

van Genuchten, M. T. (1980). A closed form equation for predicting the hydraulic conductivity of unsaturated soils. *Soil Science Society of America Journal, 44*, 892-898.

Vapnik, V., & Lerner, A. (1963). Pattern recognition using generalized portrait method. *Automation and Remote Control, 24*, 774–780.

Vukovic, M., & Soro, A. (1992). *Determination of Hydraulic Conductivity of Porous Media from Grain-Size Composition.* Littleton, Colorado: Water Resources Publications.

Whittaker, J., & Teutsch, G. (1999). Numerical simulations of subsurface characterization methods: application to a natural aquifer analogue. *Advances in Water Resources, 22*(8), 819-829.

Wilson, A. M., Huettel, M., & Klein, S. (2008). Grain size and depositional environment as predictors of permeability in coastal marine sands. *Estuarine, Coastal and Shelf Science, 80*(1), 193-199.

Wohlberg, B., Tartakovsky, D. M., & Guadagnini, A. (2006, January). Subsurface characterization with support vector machines. *IEEE Transactions on Geoscience and Remote Sensing, 44* (1).

Wolf, S. H., Celia, M. A., & Hess, K. M. (1991). Evaluation of hydraulic conductivities calculated from multiport-permeameter measurements. *Ground Water, 29*(4), 516-525.

Yang, G., & Huang, T. S. (1994, January). Human face detection in a complex background. *Pattern Recognition., 27*(1), 53–63.

Young, S. C. (1998). Impacts of positive skin effects on borehole flowmeter tests in a heterogeneous granular aquifer. *Ground Water, 36*(1), 67-75.

Zlotnik, V. A., & McGuire, V. L. (1998). Multi-level slug tests in highly permeable formations: 2. Hydraulic conductivity identification, method verification, and field applications. *Journal of Hydrology, 204*, 283-296.

Zlotnik, V. A., & Zurbuchen, B. R. (2003a). Field study of hydraulic conductivity in a heterogeneous aquifer: Comparison of single-borehole measurements using different instruments. *Water Resources Research, 39*(4), doi: 10.1029/2002WR001415.

Zlotnik, V. A., & Zurbuchen, B. R. (2003b). Estimation of hydraulic conductivity from borehole flowmeter tests considering head losses. *Journal of Hydrology, 281*, 115-128.

Zlotnik, V. A., Zurbuchen, R. F., Ptak, T., & Teutsch, G. (2000). Support volume and scale effect in hydraulic conductivity: experimental aspects. In D. Zhang, & C. L. Winter (Eds.), *Theory, Modeling, and Field Investigation in Hydrogeology: A Special Volume in Honor of Shlomo P. Neuman's 60th Birthday* (pp. 348: 215-231). Boulder, Colorado: Geological Society of America Special Paper.

APPENDIX A

BASIC STATISTICS ON D_{10} AND D_{60} SAMPLES USED FOR THE ESTIMATION OF K_{GS}

The basic sample statistics for d_{10} and d_{60} are presented in Table A1. Figure A1 shows the histograms of frequency distribution for d_{10} and d_{60}. For illustration purposes, a lognormal model based on the statistics of d_{10} and a normal distribution model based on the statistics of d_{60} are also presented. One can observe that d_{10} values show a very positively skewed distribution, while d_{60} values present a symmetric distribution.

Table A1. Basic sample statistics of d_{10} and d_{60}.

Characteristics	d_{10}	d_{60}
Number of samples	407	407
Minimum [mm]	3.91E-02	3.80E-01
Maximum [mm]	5.25E+00	4.25E+01
Mean [mm]	9.15E-01	1.37E+01
Geometric mean [mm]	6.21E-01	1.27E+01
Standard deviation [mm]	9.18E-01	4.24E+00
Skewness coefficient	2.11E+00	4.09E-01

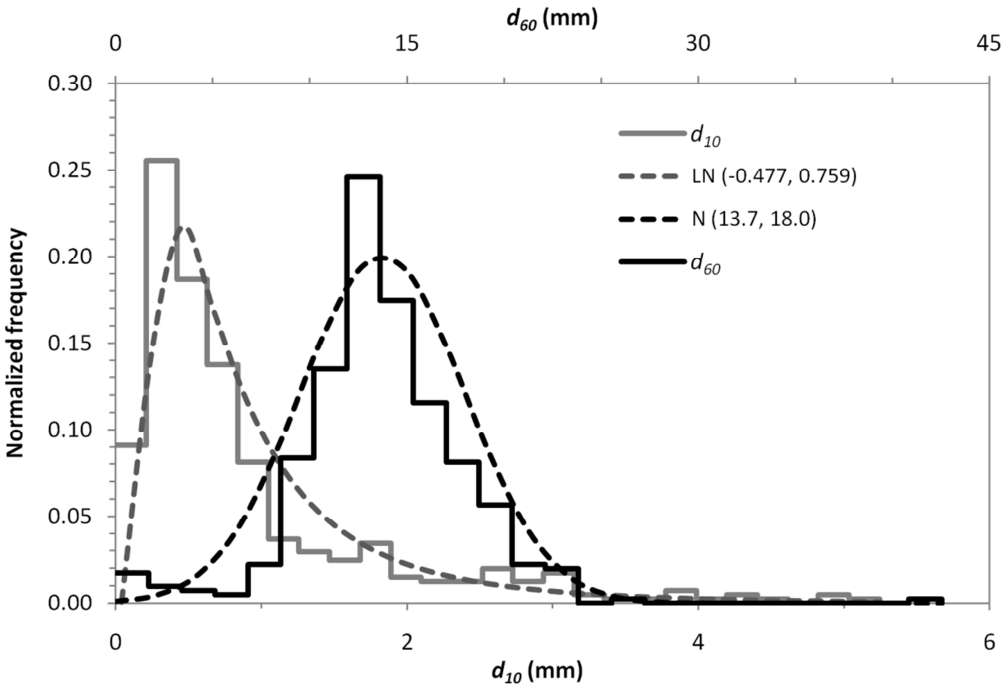

Figure A1. Histograms of frequency distribution for d_{10} (*continuous gray line*) and d_{60} (*continuous black line*) (notice the different horizontal axes). A lognormal model based on the statistics of d_{10} (*dashed gray line*) and normal distribution model based on the statistics of d_{60} (*dashed black line*) are included for illustration purposes.

Uncertainty associated with *K* estimates from grain size distributions

On the basis of equations (Equation 2.1) and (Equation 2.5) in chapter 2, the uncertainty associated with *K* estimates from grain size distributions, $u_{K_{GS}}$, can be written as

$$u_{K_{GS}} = \sqrt{\left(\frac{\partial K_{GS}}{\partial d_{10}}\right)^2 \left(u_{d_{10}}\right)^2 + \left(\frac{\partial K_{GS}}{\partial d_{60}}\right)^2 \left(u_{d_{60}}\right)^2} \tag{A1}$$

The Kozeny-Carman formulation reads

$$K_{GS} = A\frac{\phi^3}{\left(1-\phi^2\right)}d_{10}^2 \tag{A2}$$

where $A = g\ C\ /\ \nu$ is assumed to be known without uncertainty. From (Equation 2.4), it is recalled that the porosity, ϕ, can be written in terms of the uniformity coefficient, U, as

$$\phi = a\left(1+b^U\right); \qquad U = \left(\frac{d_{60}}{d_{10}}\right);\ a = 0.255;\ b = 0.83 \tag{A3}$$

Renaming $d_{60} = z$ and $d_{10} = x$, and using (A1) – (A3) leads to

$$K_{GS} = Ax^2a^3\left[\frac{\left(b^{\frac{z}{x}}+1\right)^3}{\left(1-a\left(b^{\frac{z}{x}}+1\right)\right)^2}\right] \tag{A4}$$

Taking derivative of [A4] with respect to x and z, leads to

$$\frac{dK_{GS}}{dx} = \frac{a^3A\left(b^{\frac{z}{x}}+1\right)^2\left(2x\left(b^{\frac{z}{x}}+1\right)\left(ab^{\frac{z}{x}}+a-1\right)-z\log\left(b\right)b^{\frac{z}{x}}\left(ab^{\frac{z}{x}}+a-3\right)\right)}{\left(ab^{\frac{z}{x}}+a-1\right)^3} \tag{A5}$$

$$\frac{dK_{GS}}{dz} = \frac{a^3 Ax \log(b) b^{\frac{z}{x}} \left(b^{\frac{z}{x}} + 1\right)^2 \left(ab^{\frac{z}{x}} + a - 3\right)}{\left(ab^{\frac{z}{x}} + a - 1\right)^3} \tag{A6}$$

The uncertainty associated with d_{10} and d_{60} measurements has been estimated to be less than 2% by the American Association for Laboratory Accreditation (2005). In this case, however, a conservative 2% value is used for the estimation of the uncertainty.

As an example Figure A2 shows the histogram of uncertainties for the 407 samples included in the data set. The estimated uncertainty $u_{K_{GS}}$ was less than 10% for 95% of the total number of samples.

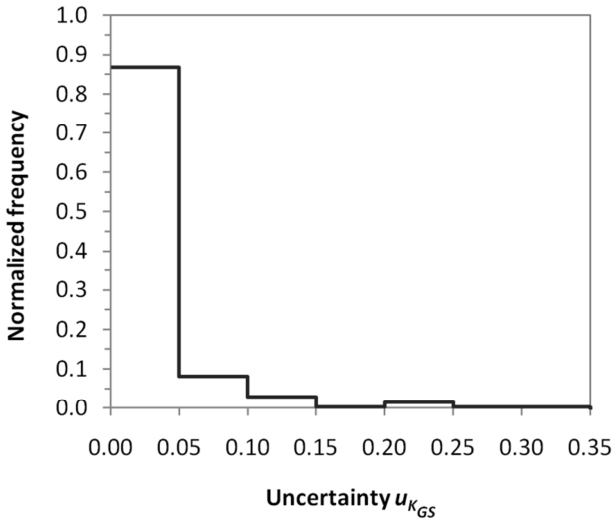

Figure A2. Histogram of frequency distribution for K_{GS} uncertainty.

References

American Association for Laboratory Accreditation (2005) P103d – Annex: Policy on Estimating Measurement Uncertainty for Construction Materials & Geotechnical Testing Labs.

APPENDIX B

THE NEAREST-NEIGHBOR CLASSIFICATION (NNC)

The nearest-neighbor classification (NNC) employed by Tartakovsky et al. (2007) is a k-nearest-neighbor classification (Hastie et al., 2001) in which the classification of a test point is determined by majority vote amongst the k nearest-neighbor points in the training set, Tartakovsky et al. (2007) considered the case in which k=1, for which the classification of each point in the domain is determined by finding the nearest training point, and assigning the known class of that point. Given a set of training data points $I_i=I(\mathbf{x}_i, F_k)$, i=1,…,n, the NNC classification for an arbitrary point **x** in the domain is computed as follows: (1) Define j as the index of the training data point, from the set $\{x_i\}_{i=1}^{N}$, which is closest to query point x; that is, $j = \mathbf{argmin}_i \|x - x_i\|_2$. Usually an Euclidean measure is prefer as distance metric, for simplicity, however, other metric can be used; (2) Assign the indicator function value of training data point x_j (i.e., $I(x_j)$) as the indicator function value of query point x. This classification is simple to compute, and has no free parameters to estimate (no optimization of the method is possible).